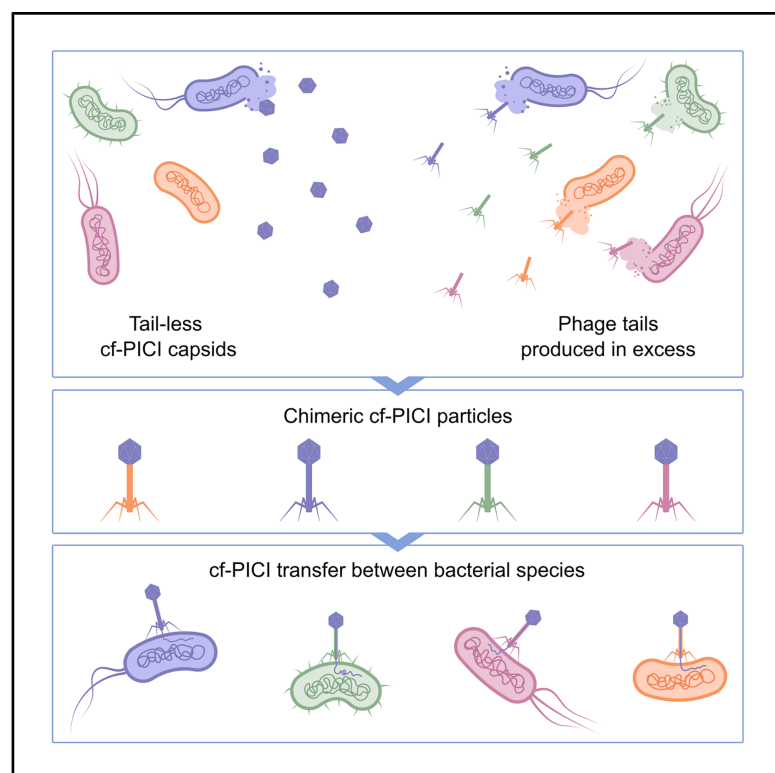


# Chimeric infective particles expand species boundaries in phage-inducible chromosomal island mobilization

## Graphical abstract



## Authors

Lingchen He, Jonasz B. Patkowski, Jinlong Wang, ..., Alfred Fillol-Salom, Tiago R.D. Costa, José R. Penadés

## Correspondence

t.costa@imperial.ac.uk (T.R.D.C.), j.penades@imperial.ac.uk (J.R.P.)

## In brief

Capsid-forming PICIs (cf-PICIs) produce their own capsids and exploit phage tails from unrelated species to transfer their DNA across bacterial hosts. This tail piracy enables broad dissemination and reveals a new mechanism of horizontal gene transfer with major implications for bacterial evolution and pathogenesis.

## Highlights

- cf-PICIs form tailless capsids, which are released into the environment
- These capsids can hijack different phage tails to form chimeric infectious particles
- Tail piracy allows cf-PICIs to cross-species barriers and spread broadly
- Structural analysis reveals unique capsid formation of cf-PICIs

Article

# Chimeric infective particles expand species boundaries in phage-inducible chromosomal island mobilization

Lingchen He,<sup>1,2,7</sup> Jonasz B. Patkowski,<sup>1,2,3,7</sup> Jinlong Wang,<sup>1,2</sup> Laura Miguel-Romero,<sup>1,4</sup> Christopher H.S. Aylett,<sup>1</sup> Alfred Fillol-Salom,<sup>1,5</sup> Tiago R.D. Costa,<sup>2,3,\*</sup> and José R. Penadés<sup>1,2,6,8,\*</sup>

<sup>1</sup>Department of Infectious Disease, Imperial College London, London SW7 2AZ, UK

<sup>2</sup>Centre for Bacterial Resistance Biology, Imperial College London, London SW7 2AZ, UK

<sup>3</sup>Department of Life Sciences, Imperial College London, London SW7 2AZ, UK

<sup>4</sup>Instituto de Biomedicina de Valencia (IBV), CSIC, 46010 Valencia, Spain

<sup>5</sup>Institute for Integrative Systems Biology, Universitat de València, CSIC, 46980 Paterna, Spain

<sup>6</sup>School of Health Sciences, Universidad CEU Cardenal Herrera, CEU Universities, 46115 Alfara del Patriarca, Spain

<sup>7</sup>These authors contributed equally

<sup>8</sup>Lead contact

\*Correspondence: [t.costa@imperial.ac.uk](mailto:t.costa@imperial.ac.uk) (T.R.D.C.), [j.penades@imperial.ac.uk](mailto:j.penades@imperial.ac.uk) (J.R.P.)

<https://doi.org/10.1016/j.cell.2025.08.019>

## SUMMARY

Some mobile genetic elements spread among unrelated bacterial species through unknown mechanisms. Recently, we discovered that identical capsid-forming phage-inducible chromosomal islands (cf-PICIs), a new family of phage satellites, are present across multiple species and genera, raising questions about their widespread dissemination. Here, we have identified and characterized a new biological entity enabling this transfer. Unlike other satellites, cf-PICIs produce their own capsids and package their DNA, relying solely on phage tails for transfer. cf-PICIs release non-infective, tailless capsids containing their DNA into the environment. These subcellular entities then interact with phage tails from various species, forming chimeric particles that inject DNA into different bacterial species depending on the tail present. Additionally, we elucidated the structure of the tailless cf-PICIs and the mechanism behind their unique capsid formation. Our findings illuminate the mechanisms used by satellites to spread in nature, contributing to bacterial evolution and the emergence of new pathogens.

## INTRODUCTION

Horizontal gene transfer (HGT) between bacterial species is crucial for bacterial evolution, environmental adaptation, antibiotic resistance spread, and pathogen emergence. Understanding these processes is essential to developing strategies to combat antibiotic resistance and mitigate the impact of bacterial pathogens on human health and the environment.

We have recently investigated a family of mobile genetic elements (MGEs) called phage-inducible chromosomal islands (PICIs).<sup>1,2</sup> These small (~10–15 kb), chromosomally integrated elements are widespread, found in over 200 species, with many strains harboring multiple copies.<sup>3</sup> PICIs parasitize certain temperate (helper) phages. Upon induction by active helper phages, PICIs replicate,<sup>4</sup> excise from the chromosome, and are efficiently packaged into infectious particles using phage virion proteins, enabling high intraspecies transfer.<sup>1</sup>

Beyond their dissemination mechanisms, PICIs significantly impact host biology. Clinically, they carry and spread virulence and resistance genes, including superantigens, host adaptation

factors, and antimicrobial resistance determinants that can convert non-pathogenic strains into pathogens.<sup>1</sup> Evolutionarily, PICIs engage in two potent gene transfer mechanisms—PICI lateral transduction and cotransduction—which drive extensive chromosomal mobility.<sup>4</sup> Combined with helper phage-mediated lateral transduction,<sup>5</sup> they can mobilize up to 70% of the chromosome in a single event.<sup>6</sup> PICIs also participate in generalized transduction.<sup>7</sup> Ecologically, they encode diverse immune systems,<sup>8</sup> influencing HGT by either promoting or restricting it. They also affect the biology of other MGEs, including phages<sup>9</sup> and plasmids.<sup>10</sup>

We recently began exploring how PICIs emerge in different species. The near absence of identical PICIs across species suggested limited interspecies mobility.<sup>3</sup> However, the discovery of capsid-forming PICIs (cf-PICIs) changed this view. Unlike other PICIs and phage satellites,<sup>2,11,12</sup> including P4,<sup>13</sup> PLE,<sup>14</sup> or PICMIs,<sup>15</sup> whose packaging depends entirely on helper phages, cf-PICIs uniquely produce PICI-sized capsids and package their DNA independently.<sup>16</sup> Once induced, they require only phage tails for transfer. To form cf-PICI capsids, the proteins



encoded by cf-PICl genes interact exclusively with other cf-PICl proteins, not phage counterparts.<sup>16</sup> The mechanisms underlying this specificity remain unknown.

In a prior study, we found cf-PICls were the most abundant satellites in nature and present in multiple host species.<sup>3</sup> We hypothesized that cf-PICls might spread across phylogenetically distant hosts by forming their own capsids that can associate with non-helper phage tails. This led us to investigate the mechanisms driving their intra- and interspecies dissemination.

Here, we show that cf-PICls, even without a helper phage, naturally produce tailless capsids containing their genome. Once released into nature, these tailless small capsids can interact with tails of phages that infect different bacterial host species, which are produced in excess during the phage lytic cycle. In turn, this creates chimeric infective particles that inject cf-PICl DNA into diverse hosts, depending on the hijacked tail—a phenomenon we term *tail piracy*. Additionally, we have elucidated the molecular details of cf-PICl capsids as a first step toward understanding how their structural features might facilitate association with diverse phage tails.

## RESULTS

### Helper phages can promote cf-PICl induction but not their transfer

During previous analyses,<sup>3,16</sup> we identified nearly identical cf-PICls in different species. Notably, one cf-PICl, EcCIGN02175 (EcCI1), was found in five genera and seven species, including *Escherichia coli*, *Klebsiella pneumoniae*, *Shigella flexneri*, *Citrobacter freundii*, *Citrobacter amalonaticus*, *Enterobacter asburiae*, and *Enterobacter hormaechei* (Figure S1; Table S1). Alongside the *E. coli* GN02175 strain carrying EcCI1, we included *K. pneumoniae* DSM30104, which harbors a highly similar island (KpCIDS030104, or KpCI1; Figure 1A).

Comparison of these islands revealed four variable regions: two flanking the operon encoding genes for cf-PICl capsid formation (the packaging module), likely encoding antiphage systems<sup>8</sup>; one downstream of *alpA*, with unknown function; and one within the packaging module, involving genes for the tail connector and adaptor proteins (Figure 1A). While KpCI1 was not found in other species, it was present in additional *K. pneumoniae* strains (Table S2).

To assess whether EcCI1 and KpCI1 could transfer between species, we first tested whether *E. coli* GN02175 and *K. pneumoniae* DSM30104 strains, carrying a tetracycline resistance marker (*tetA*) in each of the cf-PICls, contained resident prophages capable of inducing the islands. *E. coli* GN02175 carries seven prophages, and *K. pneumoniae* DSM30104 has two. Following mitomycin C (MC) induction, we collected DNA at different time points and analyzed it via agarose gel electrophoresis (Figures S2A and S2B) and Southern blotting using cf-PICl-specific probes (Figures 1B and 1C). Both strains showed signs of cf-PICl induction and packaging, with the presence of bulk DNA (indicative of replication) and a small-sized cf-PICl band (representative of packaging into small capsids; Figures 1B and 1C). These results indicated that both strains contained a helper phage for the satellites.

Due to the complexity of the *E. coli* strain (multiple prophages and an additional PICl), we focused on KpCI1. Since DSM30104 contains only two prophages (P1 and P2) and the cf-PICl, we created mutants lacking either P1 or P2. After MC induction, deletion of P1 abolished cf-PICl induction (Figures S2C and S2D) and transfer (Figure S2E), confirming P1 as the helper. The analysis of a *K. pneumoniae* DSM30104 derivative strain carrying only the helper phage revealed that the presence of the island severely affects the phage, causing a more than 100-fold reduction in phage particles in lysates with the island compared with lysates with only the phage (Figure S2F).

Next, we used the obtained lysates to test the transfer of the different islands to different species. Note that we included the *E. coli* GN02175 and *K. pneumoniae* DSM30104 strains, with scarless deletions of the cf-PICl islands, as recipients to minimize the impact of the bacterial immune system (especially restriction-modification systems) in blocking HGT. We observed low intraspecies transfer of both islands, with mean transfer frequencies of  $5.1 \times 10^3 (\pm 2.9 \times 10^3)$  colony-forming unit (CFU)/mL for EcCI1 (Figure 1D) and  $6.2 \times 10^2 (\pm 3.3 \times 10^2)$  CFU/mL for KpCI1 (Figure 1E) lysates. Note that the previous report analyzing cf-PICl found transfer frequencies of the prototypical cf-PICl island higher than  $10^6$  cf-PICl transductants/mL upon helper phage induction,<sup>16</sup> more than 2 logs higher than the results presented here. No interspecies transfer was observed, despite conservation of the attachment sites (*attB*) among the species. Both EcCI1 and KpCI1 encode identical integrases and use the same *attB* sequence (ttcatgccgta) located within the *fis* gene.<sup>17</sup> Given that both islands were induced by resident prophages, the low intraspecies transfer was unexpected.

### cf-PICls naturally produce tailless particles

Our earlier analysis of KpCI1 induction (Figure 1C) revealed that the island was both induced and packaged into small cf-PICl-sized capsids, as evidenced by a DNA band consistent with the expected size of the packaged genome. However, the absence of infective cf-PICl particles suggested that the helper phage may not supply the tails needed for full particle assembly. Supporting this, the helper phage, which has short tails, exhibits the podovirus morphotype, whereas cf-PICls use non-contractile long tails characteristic of the siphovirus.<sup>16</sup>

Due to this apparent incompatibility, and to further investigate how KpCI1 is transferred, we constructed mutants of the *K. pneumoniae* DSM30104 strain in which either the capsid gene of KpCI1 or the capsid or tail genes of the helper phage P1 were deleted. Following MC induction, we assessed island transfer. Deletion of the cf-PICl capsid gene did not impair transfer, whereas deletion of either the capsid or tail genes of P1 completely abolished production of both phage and KpCI1 infective particles (Figures S3A and S3B). These findings indicate that KpCI1 is mobilized via P1-mediated generalized transduction, independent of its own capsid production.

The previous results also suggested that, because KpCI1 was induced by a phage (P1) that cannot provide tails to complete the formation of infective KpCI1 particles, tailless KpCI1 capsids should be present in the lysate of induced cells. To test this, we isolated particles from MC-induced cultures of wild-type (WT) *K. pneumoniae* DSM30104 and derivative strains lacking P1

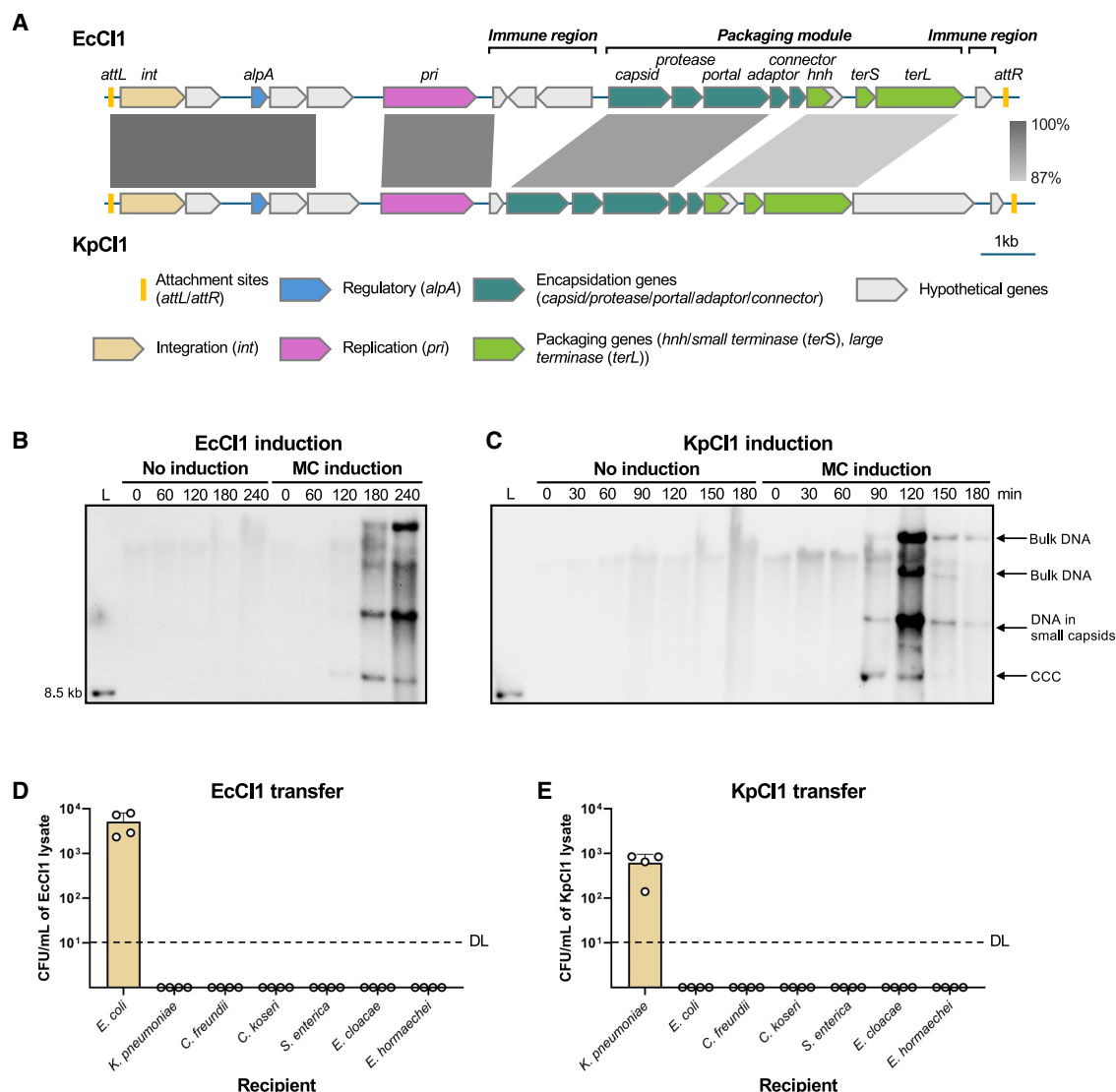


**Figure 1. Induced cf-PICs have low intraspecies transfer**

(A) A comparative map between cf-PICs EcCI1 and KpCI1. Genes are colored based on their function. Gray scales between cf-PICs indicate the regions that share similarity, identified by BLASTn.

(B and C) Induction of EcCI1 or KpCI1 by resident prophages. *E. coli* GN02175 or *K. pneumoniae* DSM30104 strains were MC-induced, and samples were taken at the indicated time points (min) for DNA analyses. DNA was separated on a 0.7% agarose gel (see Figure S2), followed by Southern blotting analysis using specific EcCI1 (B) or KpCI1 (C) probes. L, Southern blot molecular marker (DNA molecular weight marker VII; Roche). CCC, covalently closed circular.

(D and E) Transfer of EcCI1 (D) or KpCI1 (E) to different bacterial species. *E. coli* GN02175 or *K. pneumoniae* DSM30104 strains were MC-induced, and the resulting lysates were used to infect the following strains: *E. coli* JP24699, *K. pneumoniae* JP24460, *Citrobacter freundii* 2H5, *Citrobacter koseri* 2F8, *Salmonella enterica* JP18938, *Enterobacter cloacae* ATCC13047, and *Enterobacter hormaechei* Eh1\_18. Values are presented as means of the number of colony-forming units (CFUs) per milliliter of cf-PIC donor lysates. Error bars represent the standard deviation.  $n = 4$  independent samples. DLs, detection limits.

See also Figures S1 and S2 and Tables S1 and S2.

( $\Delta$ P1), the non-helper phage P2 ( $\Delta$ P2), or both KpCI1 and P1 ( $\Delta$ KpCI1  $\Delta$ P1). Packaged DNA was extracted, separated by agarose gel electrophoresis, and analyzed by Southern blot. As shown in Figure 2A, all lysates from strains containing both P1 and KpCI1 exhibited DNA packaged in small capsids, indicating that KpCI1 small capsids assemble correctly upon induction.

In lysates from the WT strain, three DNA bands of similar intensity were observed (Figure 2A). Southern blotting identified the

high-molecular-weight band as renatured cf-PIC DNA concatemers, likely formed via cohesive ends at *cos* sites, while the small-sized band corresponded to monomeric cf-PIC DNA. The intermediate band was attributed to the phage genome (Figure 2B). To quantify packaging efficiency, we sequenced DNA from WT and  $\Delta$ P2 lysates and mapped reads to the KpCI1 and P1 genomes. In both cases, KpCI1 DNA was packaged more abundantly than P1 DNA (Figures S3C–S3J). In WT

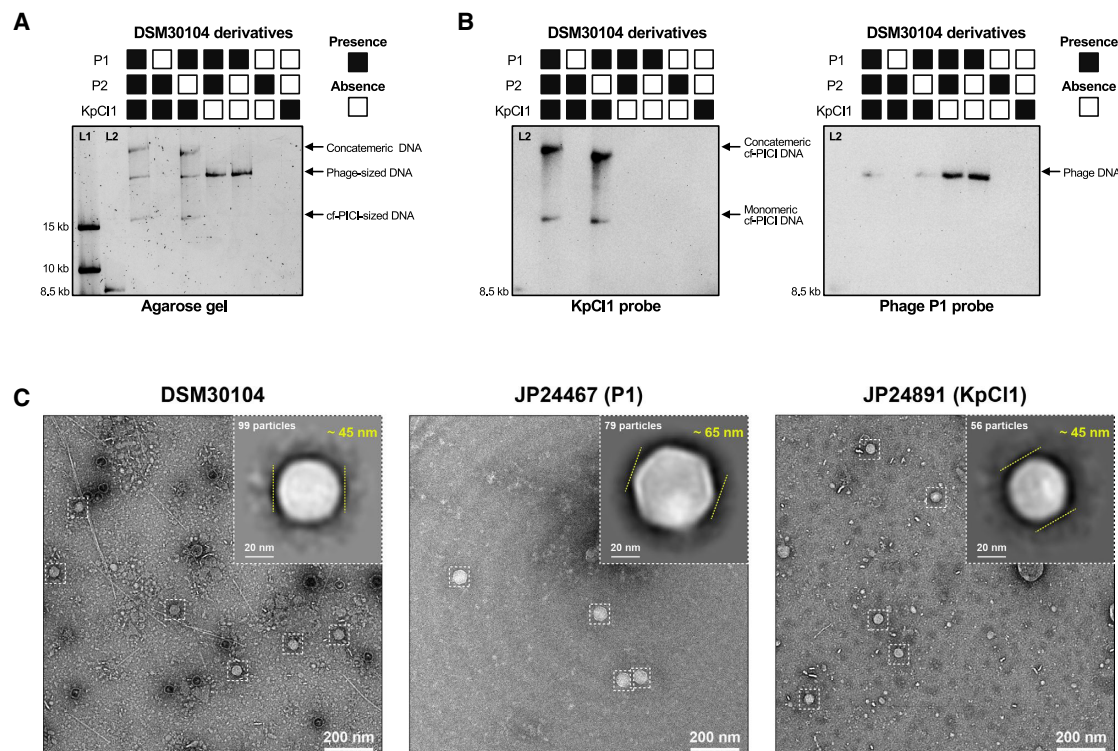


**Figure 2. cf-PICs naturally produce tailless particles**

(A) The packaged DNA extracted from lysates after induction of different DSM30104 derivative strains was separated on a 0.7% agarose gel and quantified. Black boxes indicate the presence of the element, while white boxes indicate its absence. The relative quantification of the different bands (see [STAR Methods](#)) provided the following results: in the lane of the WT sample, the mean grayscale values for the upper, middle, and lower bands were 127, 134, and 137, respectively. In the lane of the  $\Delta$ P2 sample, the mean grayscale values for the upper, middle, and lower bands were 118, 125, and 130, respectively. In the lane of the  $\Delta$ KpCI1 sample and the lane of the  $\Delta$ P2  $\Delta$ KpCI1 sample, the mean grayscale values for the P1 DNA bands were 103 and 96, respectively. Lower grayscale values correspond to higher DNA amounts. L1, invitrogen 1 kb plus DNA ladder; L2, Southern blot molecular marker (DNA molecular weight marker VII; Roche).

(B) Southern blot analyses of the samples obtained in panel A, using KpCI1- or P1-specific probes. L2, Southern blot molecular marker (DNA molecular weight marker VII; Roche).

(C) Negative-stain EM images of tailless cf-PICs. Left: micrograph showing the tailless KpCI1 capsids present in the lysate of the induced WT DSM30104 strain. The upper right corner inset represents a 2D class average of 99 manually picked particles of KpCI1, which have approximately 45 nm in diameter. Middle: micrograph showing the helper phage P1 present in the lysate of the induced DSM30104 derivative strain mutant in the cf-PIC1 KpCI1 and the P2 prophage (JP24467). P1 has a clear podovirus morphology. The upper right corner inset represents a 2D class average of 79 manually picked particles of P1 with approximately 65 nm in diameter. Right: micrograph showing the tailless KpCI1 capsids obtained after induction of the DSM30104 derivative strain mutant in P2 and in the capsid gene of P1 (JP24891). The upper right corner inset represents a 2D class average of 56 manually picked particles of KpCI1 with approximately 45 nm in diameter. Scale bars represent 200 nm (full micrographs) and 20 nm (insets).

See also [Figure S3](#).

lysates ([Figures S3E and S3F](#)), average read coverage was 10,849 for KpCI1 versus 1,829 for P1. In the  $\Delta$ P2 strain ([Figures S3I and S3J](#)), the coverage was 8,923 for KpCI1 and 3,865 for P1. Moreover, the coverage plots further supported the nature of each element: KpCI1, a cos-type element, displayed a valley-shaped coverage profile ([Figures S3E and S3I](#)), while P1, a pac-type phage capable of generalized transduction, showed a mountain peak-like pattern ([Figures S3F and S3J](#)). Together, these results confirm that (1) KpCI1 efficiently packages its DNA upon induction, (2) it does so at the expense of phage reproduction, and (3) packaging is independent of the phage capsid, which is instead essential for transduction.

Notably, no packaged DNA was detected in lysates from the strain containing only the non-helper phage P2 ( $\Delta$ KpCI1  $\Delta$ P1), suggesting that P2 is either non-functional or not inducible by

the SOS response ([Figure 2A](#)). In support of the latter option, it is similar to *E. coli* phage P2,<sup>18</sup> which is not induced after treatment of the P2 lysogen with MC. The absence of packaged cf-PIC1 DNA in P1 deletion mutants further confirmed that P1 is the helper responsible for KpCI1 activation ([Figures 2A and 2B](#)).

To corroborate that P1 is not required for cf-PIC1 DNA packaging, we repeated the assay using strains with WT or mutant versions of P1 and KpCI1. While the absence of the P1 capsid did not affect KpCI1 packaging, mutation of the KpCI1 capsid gene completely abolished its packaging ([Figure S3K](#)), confirming the ability of the cf-PICs to package their DNA independently of the inducing phage.

Finally, to determine whether the packaged cf-PICs contain tails, we examined lysates from induced WT *K. pneumoniae* DSM30104 by negative-stain transmission electron microscopy

(EM). As controls, we also examined lysates from a strain lacking KpCI1 and P2 (producing only P1, JP24467) and from a strain lacking P1 capsid and P2 (producing only KpCI1 particles, JP24891). Tailless KpCI1 particles were observed in the WT and JP24891 samples, but not in the P1-only lysate, which exhibited podovirus morphology (Figure 2C).

To better characterize particle morphology, we acquired 200 micrographs from WT DSM30104, 26 from JP24467 (P1 only), and 98 from JP24891 (KpCI1 only). From these, we selected a large number of particles for measurement:  $n = 99$  KpCI1 particles from strain DSM30104,  $n = 79$  P1 particles from strain JP24467, and  $n = 56$  KpCI1 particles from strain JP24891. We then performed 2D classification averaging, which aligns and averages similar particles to yield accurate diameter measurements. Representative class averages and raw micrographs are shown in Figure 2C. These results demonstrate that KpCI1 is released as a non-infective particle lacking tails, despite being efficiently packaged. This reveals a new mode of satellite-helper interaction, where the helper phage induces the island and lyses the host but fails to supply the tails required for forming complete infective cf-PICl particles. Our findings suggest that some cf-PICls may require two helper phages: one to induce the island and another to supply tails for infectious particle assembly.

### The formation of hybrid infective cf-PICls promotes intra- and intergeneric transfer

The previous findings raised an important question: what happens to the tailless cf-PICl particles released after induction? Are they merely discarded, or do they represent a new type of biological entity with an as-yet-undetermined function?

In bacterial cells, the packaging of phage or satellite DNAs into large or small capsids, respectively, and the formation of phage tails occur concurrently but independently.<sup>19</sup> Once DNA is packaged and the capsids mature, pre-formed tails attach to the capsids to create infective phage or satellite particles. It is also well known that the host range of a phage or PICl is primarily determined by the tail fibers (or spikes), which mediate the initial, reversible, and specific recognition and adsorption of susceptible bacteria.<sup>20</sup> Tail receptors are typically species- or even strain-specific, explaining the narrow host range of both phages and their satellites. Since previous studies suggested that phage tails are produced in excess during the phage lytic cycle,<sup>21</sup> we hypothesized that cf-PICl capsids, once released, could interact with free tail fibers from phages infecting different species. This interaction could generate chimeric particles with altered host ranges, thereby providing a biological rationale for the production of tailless cf-PICl capsids and their potential for interspecies transfer.

To test this, we MC-induced the clinical isolate *K. pneumoniae* DSM30104 ΔP2 (JP24853), whose lysate predominantly contains tailless KpCI1 particles (Figure 2). In parallel, we induced lysogenic *E. coli* strains carrying capsid mutant versions of the phages HK106 or HK022, both of which encode distinct tail structures (Figure S4A). These phages were previously used to characterize cf-PICls in *E. coli*.<sup>16</sup> The resulting lysates from these mutants contained only phage tails. We then mixed the *K. pneumoniae* KpCI1 lysate with the *E. coli* tail-containing lysates at a 1:1 ratio and tested for transfer of the KpCI1 cf-PICl to various species.

While intraspecies transfer remained unchanged, the presence of HK022-derived tails enabled highly efficient intergeneric transfer of KpCI1 into *E. coli* strain C1a. Transfer occurred at a mean frequency of  $2.3 \times 10^7 (\pm 2.4 \times 10^6)$  CFU/mL of KpCI1 lysate (Figure 3A)—a rate rarely observed for other satellite elements. No transfer was observed in the absence of tails or in the presence of HK106 tails, suggesting that compatibility between cf-PICl capsids and phage tails is tail-type dependent. Although similar high-frequency transfer was detected in other *E. coli* strains, no transfer was observed to more distantly related species (Figure 3B), consistent with the notion that phage tails dictate host tropism. These results suggest that KpCI1 capsids can assemble with HK022 tails to form functional hybrid particles capable of DNA delivery into *E. coli* (Figure 3B).

To confirm full-island transfer, we conducted PCR analyses on 16 independent *E. coli* recipient strains (Figures S4B–S4F) and performed Nanopore long-read sequencing on three of them. These analyses confirmed the successful integration of the entire KpCI1 element at its cognate *attB* site in the *E. coli* genome. Furthermore, the existence of chimeric infective particles was confirmed by EM (Figure 3C). In this experiment, we also imaged native HK022 phages, allowing a clear comparison between the smaller KpCI1 chimeric capsids (~45 nm) and the larger HK022 phages (~60 nm) (Figure 3C).

Since in the previous experiment we used *E. coli* lysates uniquely containing tails (Figures 2A and 2B), we tested whether these chimeric particles were also produced in the presence of functional *E. coli* phages (used again as tail donors). To do that, we repeated the same experiment, but now mixing the *K. pneumoniae* JP24853 lysate with the lysates obtained after induction of the *E. coli* strain carrying the WT version of the HK022 prophage. Remarkably, the interspecies transfer of the KpCI1 occurred at the same level as when the phage capsid mutants, but not the phage tail mutants, were used (Figure 3D), confirming that phage tails are produced in excess during the phage lytic cycle.<sup>21</sup>

To test whether cf-PICls could hijack tails from fully assembled, infective phages, we diluted the HK022 lysate to  $10^6$  plaque-forming unit (PFU)/mL and mixed it with tailless KpCI1 capsids ( $10^8$  capsids/mL). If KpCI1 were appropriating tails from mature phage particles, we expected to observe a reduction in phage titer. However, phage titers remained unchanged (Figures S4I and S4J), indicating that cf-PICls do not compete for or remove tails from intact phages. Instead, cf-PICls appear to rely on the excess of unassembled tails present in phage lysates (Figure S4K). Taken together, these results support a model in which tailless cf-PICl particles utilize excess tails produced during phage induction to form infective hybrid particles. This strategy enables their interspecies transfer and likely represents a natural and efficient mechanism of dissemination.

### Formation of tailless cf-PICl capsids occurs widely in nature

Are the results obtained with KpCI1 an exception, or do they reflect the general biology of cf-PICl elements? To address this question, we analyzed two clinical *E. coli* strains that naturally carry cf-PICls. One is the aforementioned *E. coli* GN02175, while



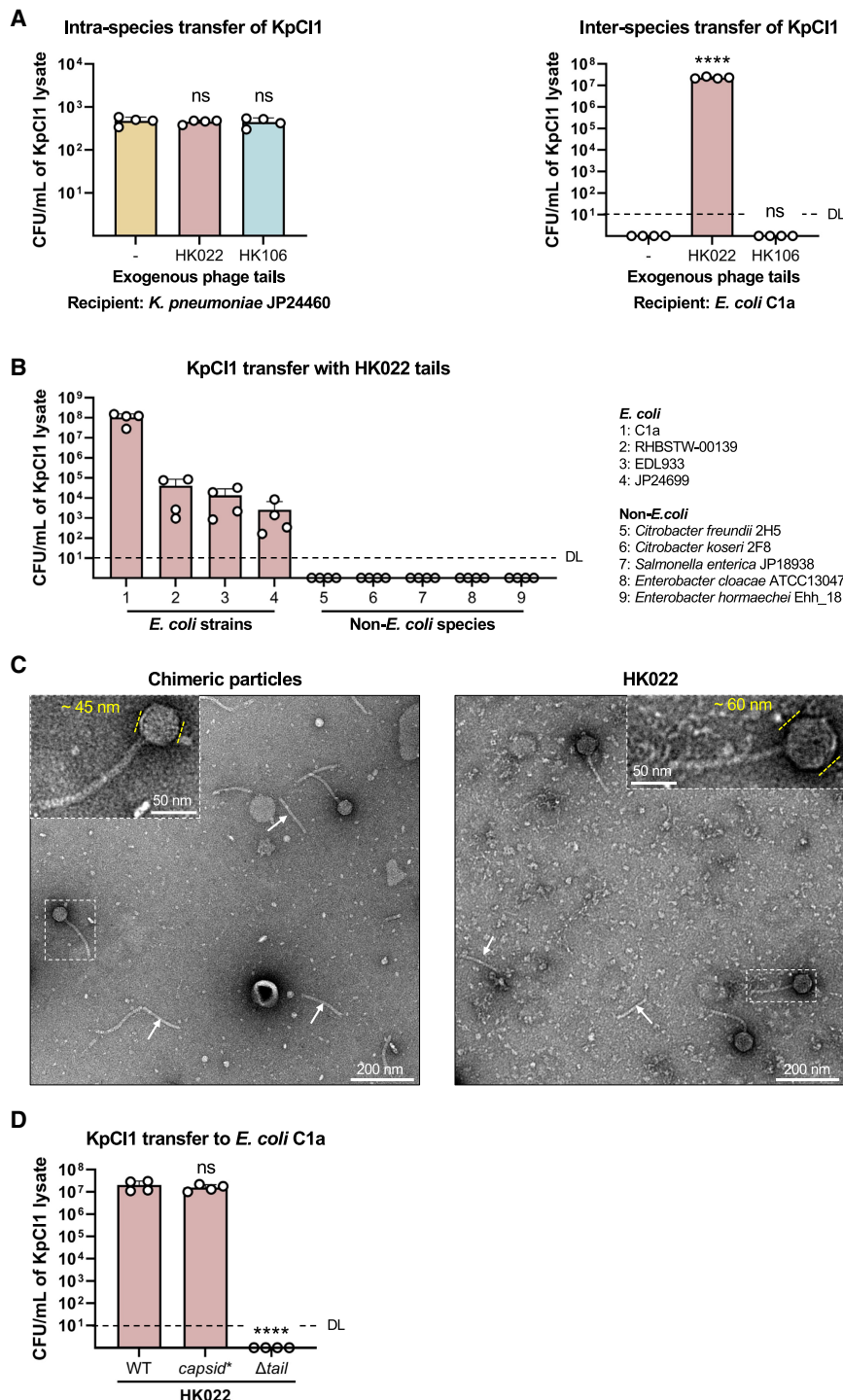


**Figure 3. Formation of chimeric cf-PICIs promotes intergeneric transfer**

(A) Intra- or interspecies transfer of KpCI1 by the formation of chimeric infective particles. The lysate obtained after induction of the *K. pneumoniae* DSM30104 ΔP2 strain (JP24853) was mixed with the lysate obtained after induction of the HK022 or HK106 prophages, mutants in their respective capsid genes. Then, the transfer of the KpCI1 island to *K. pneumoniae* JP24460 (left) or *E. coli* C1a (right) was evaluated. Values are presented as means of CFU per milliliter of cf-PICI lysates. Error bars indicate the standard deviation. A t test was used to compare the means of control and samples with additional phage tails after log<sub>10</sub> transformation. ns,  $p > 0.05$ . \*\*\*\* $p \leq 0.0001$ .  $n = 4$  independent samples. “-” represents the control where cf-PICIs were mixed with LB. DLs, detection limits.

(B) The chimeric particles have a host range that depends on the hijacked tails. The lysate containing the tailless KpCI1 particles was mixed with HK022 tails, and the transfer of KpCI1 to different species was evaluated. Recipients were *E. coli* (C1a, RHBSTW-00139, EDL933, and JP24699), *Citrobacter freundii* 2H5, *Citrobacter koseri* 2F8, *Salmonella enterica* JP18938, *Enterobacter cloacae* ATCC13047, and *Enterobacter hormaechei* Eh1\_18. Values are presented as means of CFU per milliliter of cf-PICI donor lysates. Error bars indicate the standard deviation.  $n = 4$  independent samples. DLs, detection limits.

(C) Left: negative-stain EM image of KpCI1 after incubation with HK022 phage tails, yielding fully assembled infective particles. Right: comparable negative-stain EM of WT HK022 phage. The diameters of capsids are marked in yellow. Excess free HK022 tails are highlighted with white arrows. Scale bars represent 200 nm (full micrographs) and 50 nm (insets).

(D) Induction of WT phage HK022 produces tails in excess for the intergeneric transfer of KpCI1. The lysates obtained after induction of the *K. pneumoniae* JP24853 strain (ΔP2) were mixed with the lysates obtained after induction of the WT *E. coli* HK022 lysogen or with lysates obtained after induction of the HK022 prophage mutant in genes encoding the capsid or major tail proteins. Then, the transfer of KpCI1 to *E. coli* C1a was evaluated. Values are presented as means of CFU per milliliter of cf-PICI donor lysates. Error bars indicate the standard deviation. After log<sub>10</sub> transformation, a one-way ANOVA was conducted, followed by a Dunnett’s multiple comparisons test to compare the sample with exogenous WT HK022 lysate to other samples.  $n = 4$  independent samples. ns,  $p > 0.05$ . \*\*\*\* $p \leq 0.0001$ . WT, wild type. capsid\*, mutation generated by introducing a stop codon in the capsid gene.

See also Figure S4.

the other is *E. coli* EDL933. In addition to the prototypical EcCI2DL933 (hereafter EcCI2), previously used to characterize cf-PICI elements,<sup>16</sup> EDL933 harbors 17 additional prophages.<sup>22</sup> Notably, none of these resident prophages induce the island or provide compatible tails to the EcCI2 capsids (assuming capsid

formation occurs without induction). Indeed, only a few EcCI2 transductants were previously obtained from lysates produced after MC induction of the EDL933 strain.<sup>16</sup> Both *E. coli* GN02175 and EDL933 were MC-induced, and the resulting lysates were mixed with those from *E. coli* strains carrying WT

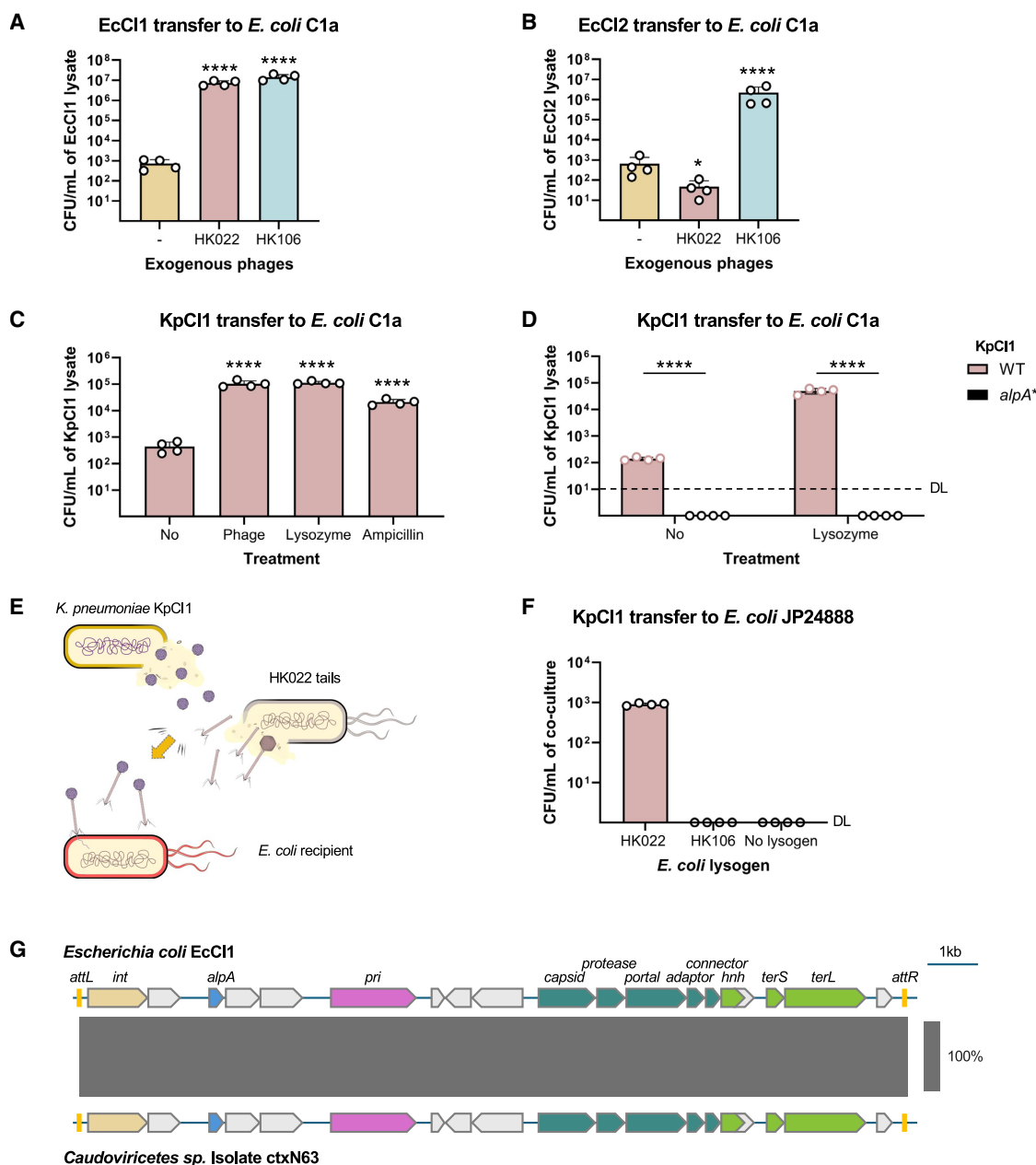


**Figure 4. Tailless cf-PICs are frequently released into natural environments and transmit within microbiota**

(A and B) Intraspecies transfer of EcCI1 (A) or EcCI2 (B) to *E. coli* C1a. Clinical *E. coli* GN02175 and EDL933 strains, carrying EcCI1 or EcCI2, respectively, were MC-induced, and the resulting lysates were tested for cf-PIC transfer in the presence or absence of lysates obtained after induction of the WT HK106 or HK022 lysogens. Values are presented as means of CFU per milliliter of cf-PIC donor lysates. Error bars indicate the standard deviation. "-" represents the control where cf-PICs were mixed with LB. A t test was used to compare the data between samples with no exogenous phage (control) and other samples after log<sub>10</sub> transformation. \**p* ≤ 0.05. \*\*\*\**p* ≤ 0.0001. *n* = 4 independent samples.

(C) cf-PICs are produced in the absence of an inducing helper prophage. The non-lysogenic *K. pneumoniae* JP24871 strain, carrying KpCI1, was grown until OD<sub>600</sub> = 0.2. Then, the strain was cultured in the presence of lytic phage K68 QB (MOI = 0.01), lysozyme (500 μg/mL), or ampicillin (50 μg/mL) at 80 rpm and 30°C for 4 h, followed by incubation at 25°C without shaking overnight. As a control, non-treated cells were also grown. The resulting lysates were filtered and mixed with HK022 lysates and tested for transfer of KpCI1 to *E. coli* C1a. Values are presented as means of CFU per milliliter of cf-PIC donor lysates. Error bars indicate the standard deviation. A t test was used to compare the data between non-treated samples and the other samples after log<sub>10</sub> transformation. \*\*\*\**p* ≤ 0.0001. *n* = 4 independent samples.

(D) AlpA is required for the formation of cf-PICs in the absence of helper phage. The non-lysogenic *K. pneumoniae* strain carrying the WT KpCI1 (JP24871) or its derivative *alpA* mutant (JP25543) was used to repeat the experiments from (C) under non-treated and lysozyme-treated conditions. The resulting filtered lysates were mixed with HK022 lysates and tested for KpCI1 transduction to *E. coli* C1a. Values are presented as means of CFU per milliliter of cf-PIC donor lysates. Error

(legend continued on next page)



HK106 or HK022 prophages. We then measured the transfer of the cf-PICIs to *E. coli* C1a.

In the absence of exogenous tails, transfer of EcCI1 was low (Figure 4A). Whether this limited transfer reflects rare events of generalized transduction or the occasional provision of tails by resident prophages remains unclear and is under investigation. Strikingly, the presence of phage tails, whether from HK106 or HK022, led to a significant ( $\sim 4$ -log) increase in EcCI1 transfer (Figure 4A), indicating that, as with KpCI1, EcCI1 produces tailless capsids upon induction. Interestingly, whereas KpCI1 only interacted with HK022 tails, EcCI1 was also able to use HK106 tails, suggesting broader tail compatibility (see below).

Previous results showed that EcCI2 is not induced by any of the resident prophages in EDL933.<sup>16</sup> However, upon adding HK106 or HK022 tails to the lysate of MC-induced EDL933, a marked increase in EcCI2 transfer was observed (Figure 4B). In this case, only the HK106 tails generated infective particles, indicating that EcCI2 tailless capsids are produced at significant levels even in the absence of helper phage induction. These capsids are likely released following cell lysis mediated by non-inducing resident prophages.

To determine whether cf-PICI capsids can form in the complete absence of a prophage, we turned to the non-lysogenic *K. pneumoniae* JP24871 strain, which exclusively harbors KpCI1. We exposed this strain to natural or biological agents known to compromise the bacterial cell wall: a lytic *K. pneumoniae* phage that does not induce the island (K68 QB), lysozyme, or  $\beta$ -lactam antibiotics. These stressors are prevalent in natural settings such as the gut, where lytic phages are present, lysozyme is secreted by Paneth cells,<sup>23</sup> and some competitors or treatments provide ampicillin. After these treatments, and in the presence of compatible tails, KpCI1 was efficiently transduced into *E. coli* C1a (Figure 4C), supporting the idea that cf-PICI capsids are spontaneously produced in the absence of helper phages.

To better understand the mechanism enabling this spontaneous production, we investigated the role of the cf-PICI-encoded *alpA* gene. In Gram-negative PICIs, including cf-PICIs, helper phages activate expression of *alpA*, which in turn initiates the PICI cycle.<sup>11</sup> We hypothesized that basal expression of *alpA* might be sufficient to trigger capsid formation even in the absence of a helper phage. Supporting this, mutation of *alpA* abolished both the production of tailless capsids and the transfer of the island in the presence of HK022 tails (Figure 4D).

In summary, these results demonstrate that cf-PICIs are frequently packaged into tailless capsids within bacterial populations, ready to exploit phage tails when available, even in the absence of infecting phages. This behavior is unique among known satellite elements and highlights the biological significance of tailless cf-PICI particles: they act as incomplete delivery systems pre-adapted to hijack phage tails from diverse sources. This promiscuous strategy expands the host range for DNA transfer and promotes widespread dissemination of cf-PICIs in natural environments.

### Interspecies cf-PICI transfer occurs naturally in mixed populations

The observation that cf-PICIs are efficiently transferred in the presence of compatible tails led us to ask whether such transfer could also occur under more natural conditions, specifically, in mixed bacterial populations grown without artificial induction of resident prophages. It is noteworthy that many bacterial species carrying identical cf-PICIs coexist as part of the gut microbiota, suggesting potential for natural interspecies transfer. To explore this possibility, we established a co-culture system involving three strains: (1) *K. pneumoniae* JP24853, which carries both the helper phage P1 and the KpCI1 island; (2) *E. coli* JP24850, lysogenic for phage HK022, which serves as the tail donor for KpCI1; and (3) *E. coli* JP24888, which harbors the non-transmissible plasmid pBAD18-*kmR* and acts as the recipient strain. Our working hypothesis was that during co-culture, the *K. pneumoniae* strain would spontaneously release tailless KpCI1 capsids, which could then acquire tails from HK022 particles released by the *E. coli* lysogen. These newly formed infective particles would subsequently transduce the KpCI1 island into the recipient *E. coli* strain (Figure 4E). Supporting this model, we observed efficient transfer of the KpCI1 island into *E. coli* JP24888 under these conditions (Figure 4F). Integration of the island was confirmed by PCR analysis, with all 16 tested colonies yielding positive results (Figures S4B and S4G). To validate the requirement for compatible tails, we repeated the experiment using an *E. coli* strain lysogenic for phage HK106 in place of the HK022 lysogen. In this case, no transfer of the KpCI1 island was detected (Figure 4F), consistent with the tail incompatibility observed between KpCI1 and HK106.

### Packaged cf-PICIs in gut microbiota

Taking into account our previous experiments, along with the fact that EcCI1 was present in different species colonizing the same niche, the human gut, we were prompted to test the

bars indicate the standard deviation. A t test was used to compare the data between WT samples and *alpA* mutant samples after  $\log_{10}$  transformation. \*\*\*\* $p \leq 0.0001$ .  $n = 4$  independent samples. DLs, detection limits.

(E) A schematic map representing the intergeneric transfer of cf-PICI KpCI1 in a mixed population, where the strain carrying KpCI1 produces tailless cf-PICIs, which will bind to the tails produced by the HK022 lysogen to form infective particles capable of mobilizing KpCI1 to a different *E. coli* recipient strain. Illustration adapted from Biocions.

(F) Interspecies transfer occurs naturally in mixed populations. *K. pneumoniae* JP24853, carrying both P1 and KpCI1, was co-cultured with either the *E. coli* HK022 or HK106 lysogens in the presence of the *E. coli* strain JP24888, used here as the recipient for KpCI1. Strains were mixed at a ratio of 1:1:1 for 5 h and then plated in the presence of both kanamycin (for JP24888) and tetracycline (for KpCI1). Values are presented as means of colony-forming units (CFUs) per milliliter of co-culture. Error bars indicate the standard deviation.  $n = 4$  independent samples. DLs, detection limits.

(G) Presence of cf-PICI EcCI1 in human metagenome studies. Genes are colored according to their sequence and function. Gray scales between cf-PICI sequences indicate regions of similarity identified by BLASTn. The overall identity between both islands is 99.95%.

See also Figure S4 and Table S3.

possibility that these islands were not only identified in the resident bacteria but also packaged as viral particles as a precursor to intergeneric transfer. Indeed, this was the case: an identical cf-PICl to EcCl1 (Figure 4G) was reported in a study that identified tens of thousands of viruses from human metagenomes associated with chronic diseases.<sup>24</sup> Moreover, we identified another 79 cf-PICl elements (Table S3) from different virome studies, confirming that the presence of packaged cf-PICl DNA occurs frequently in nature. Whether these cf-PICl particles are tailless or chimeric remains to be determined.

### Expanding cf-PICl intra- and interspecies transfer to other bacterial systems

To confirm the biological relevance of cf-PICls in gut-associated species (Table S3) and to extend our previous demonstration that KpCl1 can be mobilized from *K. pneumoniae* to *E. coli* (Figure 3B), we tested whether the cf-PICl found in *E. coli* strain GN02175 (EcCl1) could be transferred to *Enterobacter hormaechei* Eh<sub>18</sub>,<sup>25</sup> a species frequently found in the human gut. This recipient strain was selected because it harbors five prophages (potential tail donors) and a resident cf-PICl, EhClEh<sub>18</sub>, which is highly similar to EcCl1 (Figure S5A), suggesting that it could be a compatible host. To avoid interference between different cf-PICl elements, we deleted the resident EhClEh<sub>18</sub> from the *E. hormaechei* recipient strain (JP25170). The *E. coli* GN02175 and *E. hormaechei* JP25170 strains were MC-induced separately, and the resulting lysates were mixed. This approach enabled the successful transfer of EcCl1 into *E. hormaechei* JP25170 (Figure 5A). Integration into the *attB* site of the recipient genome was confirmed by PCR (Figures S4B and S4H) and by Nanopore long-read sequencing.

We next hypothesized that once established in *E. hormaechei*, EcCl1 could be further mobilized within this species. Notably, *E. hormaechei* Eh<sub>18</sub> contains prophages capable of providing compatible tails for EcCl1 (Figure 5A). To test this, we MC-induced the EcCl1-containing *E. hormaechei* strain JP25149 (which retains its resident prophages) and measured the transfer of EcCl1 into *E. hormaechei* JP25170 ( $\Delta$ EhClEh<sub>18</sub>). As expected, we observed high-frequency transfer within the species (Figure 5B). We then tested whether EcCl1 could transfer back to *E. coli*. No transfer was detected when *E. coli* was used as the recipient (Figure 5C), indicating that the prophages of *E. hormaechei* do not produce tails compatible with *E. coli*. However, when the lysate from induced *E. hormaechei* JP25149 was supplemented with tails from *E. coli* phage HK106, efficient transfer of EcCl1 back to *E. coli* was restored (Figure 5C). Finally, to broaden our observations, we showed that the KpCl1 island, when present in *E. coli* GN02175, can also be efficiently transferred to *E. coli* C1a, particularly in the presence of HK022 tails (Figure 5D).

Altogether, these results demonstrate that cf-PICls can be transferred both intra- and interspecies, provided compatible tails are present. They highlight the potential of tailless cf-PICls as naturally occurring vehicles for DNA mobilization across diverse bacterial hosts.

### cf-PICl capsids evolve to interact with different tails

Although KpCl1 and EcCl1 share high identity in their packaging modules (Figure 1A), they require different phage tails to form

infective particles. To investigate the basis for this difference, we focused on the head-tail adaptor and connector proteins, which are likely key determinants of tail compatibility. While both islands encode these proteins, the sequences differ significantly, sharing only 50% and 83% identity for the adaptor and connector proteins, respectively (Figures S5B and S5C). We hypothesized that these differences govern the ability of cf-PICl capsids to interact with specific phage tails.

To test this hypothesis, we cloned the adaptor and connector genes from both EcCl1 and KpCl1 under the control of the pBAD promoter. We also included the corresponding genes from EcCl2, a related element that encodes adaptor and connector proteins even more divergent from those in KpCl1 (35% and 63% identity) and EcCl1 (40% and 61% identity; Figures S5B and S5C). Notably, EcCl2 only interacts with tails from phage HK106 and not with those from HK022 (Figure 4B). These constructs were introduced into a *K. pneumoniae* DSM30104 derivative lacking the native KpCl1 adaptor and connector genes (strain JP24930). Following induction with MC and L-arabinose, lysates were mixed 1:1 with lysates from either phage HK022 or HK106. Expression of different adaptor and connector combinations led to differential abilities of the mutant KpCl1 to form infective particles using the various phage tails (Figure 5E). The results were consistent with previous observations (Figures 3A, 4A, and 4B), as summarized in Figure 5F: the KpCl1 mutant could use HK022 tails when expressing KpCl1- or EcCl1-derived proteins but used HK106 tails when expressing adaptor and connector proteins from EcCl2 or EcCl1.

To generalize these findings, we performed a broader genomic survey to identify highly similar cf-PICls that differed in their adaptor and connector genes. As shown in Figures S1 and S5D, we found examples of nearly identical cf-PICls that diverged only in these two genes. This reinforces the conclusion that the head-tail adaptor and connector genes are critical determinants of phage tail specificity, enabling cf-PICls to interact with a range of phage-derived tails.

### Overall architecture of the tailless cf-PICl

The capacity of cf-PICls to expand their host range stems from their ability to produce tailless, small capsids that specifically package cf-PICl DNA. The packaging operon in cf-PICls derives from phages that use the prototypical *E. coli* phage HK97 packaging system.<sup>16</sup> Notably, HK97 has served as a model system for studying phage capsid assembly and maturation for decades.<sup>26,27</sup> How cf-PICl proteins evolved to assemble only small capsids and thereby avoid interfering interactions with helper phage components remains unknown. To address this, we used cryo-electron microscopy (cryo-EM) to determine the structure of a cf-PICl particle.

We focused on EcCl2, a prototypical cf-PICl in *E. coli*. The host strain (JP24598), carrying both EcCl2 and the helper prophage HK106, was induced with MC. To prevent formation of the phage capsid, we used an HK106 derivative with a mutation in the capsid gene (*gp05*<sup>\*</sup>). As a result, only infective EcCl2 particles, and not phage particles, were produced.<sup>16</sup> The lysate was precipitated and purified by CsCl density gradient ultracentrifugation. Given the large excess of free HK106 tails typically present in such preparations, we further purified the EcCl2

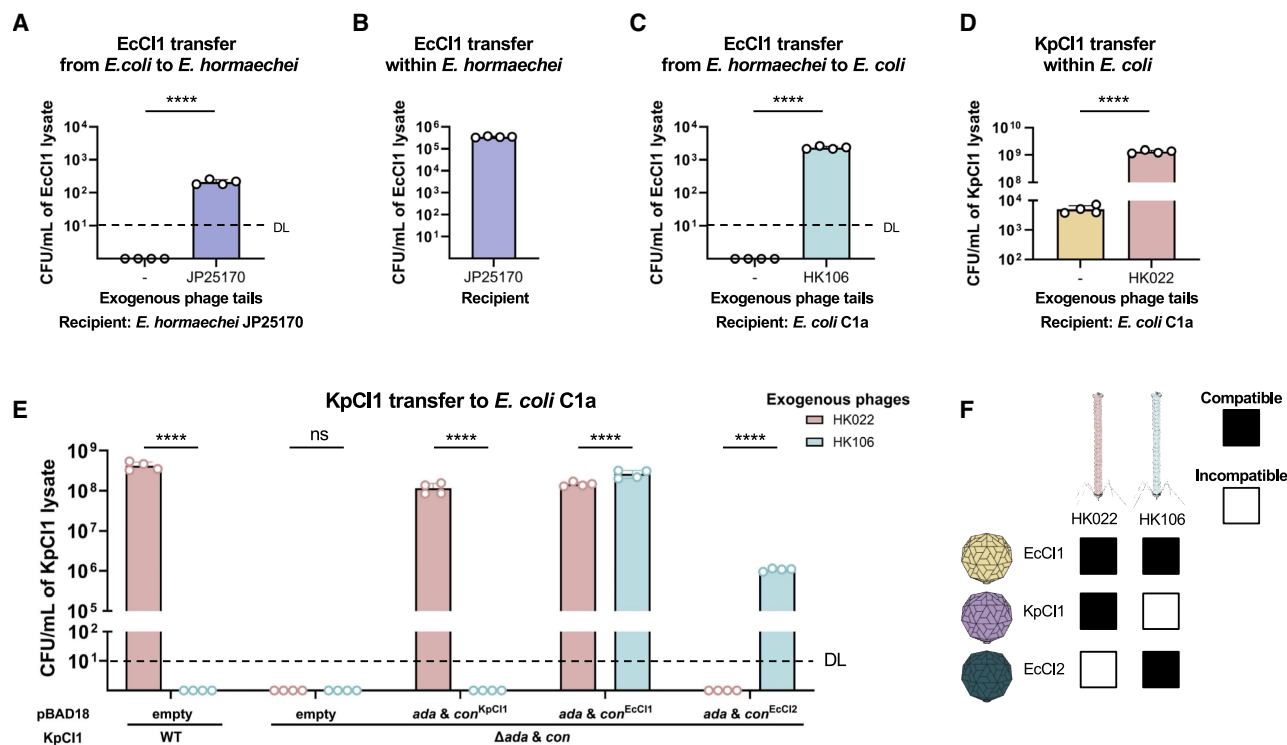


**Figure 5. The cf-PICl-encoded tail adaptor and connector proteins determine tail specificity**

(A) Interspecies transfer of EcCI1 from *E. coli* GN02175 to *E. hormaechei* JP25170 (Ehh\_18  $\Delta$ EhCIEhh\_18). The *E. coli* strain GN02175 was induced, and the lysate was mixed with the lysate obtained after MC induction of *E. hormaechei* JP25170. The transfer of EcCI1 was quantified. No transfer was observed in the absence of the *E. hormaechei* JP25170 lysate. “-” represents the control where the *E. coli* GN02175 lysate containing EcCI1 was mixed with LB.

(B) Intrasppecies transfer of EcCI1. The *E. hormaechei* JP25149 strain carrying EcCI1 was induced, and the transfer of the island to *E. hormaechei* JP25170 was analyzed.

(C) Interspecies transfer of EcCI1 from the *E. hormaechei* JP25149 to *E. coli* C1a. The *E. hormaechei* JP25149 strain carrying EcCI1 was induced, and the lysate was mixed with the lysate obtained after induction of the HK106 prophage and used to infect *E. coli* C1a.

(D) Intrasppecies transfer of KpCI1 in *E. coli*. The lysate obtained after induction of the *E. coli* GN02175 derivative JP25235, carrying KpCI1, was mixed with the lysate obtained after induction of the HK022 prophage, and the transfer of the island was analyzed. “-” represents the cf-PICl sample with no phage lysate added. In (A)–(D), values are presented as means of CFU per milliliter of cf-PICl donor lysates. Error bars indicate standard deviation.  $n = 4$  independent samples. A  $t$  test was used after a  $\log_{10}$  transformation. \*\*\*\* $p \leq 0.0001$ .

(E) cf-PICls evolve their adaptor and connector proteins to interact with different phage tails. The strain carrying KpCI1 mutated in its adaptor and connector genes ( $\Delta ada$  &  $con$ ) was complemented with different adaptor and connector genes from other cf-PICls. These strains were MC- and L-arabinose-induced. The resulting lysates were tested for KpCI1 transfer in the presence of the lysates obtained after induction of the HK022 or HK106 prophages. *E. coli* C1a was used as the recipient strain in these experiments. Values are presented as means of CFU per milliliter of cf-PICl donor lysates. Error bars indicate standard deviation. A two-way ANOVA with Sidak’s multiple comparisons test was performed after a  $\log_{10}$  transformation. \*\*\*\* $p \leq 0.0001$ .  $n = 4$  independent samples. *ada* & *con*, adaptor and connector genes; DLs, detection limits.

(F) A summary table of the compatibility between cf-PICl capsids and phage tails. Colors indicate whether the cf-PICl capsid can (black) or cannot (white) interact with the tail to form chimeric infective particles.

See also Figures S4 and S5.

particles by anion-exchange chromatography (Figure S6A), monitoring separation by SDS-PAGE (Figure S6B) and negative-stain EM (Figure S6C). This step effectively removed free tails, which bind weakly to the resin, enriching for fully assembled cf-PICl particles. Mass spectrometry of purified EcCI2 virions identified the major capsid protein (MCP) as the product of gene 1786.<sup>16</sup> This protein undergoes N-terminal cleavage, yielding a mature 32.6 kDa MCP spanning residues 93–327 (Figure 6A). The structural integrity of the infective particles was first assessed by negative-stain EM (Figure 6B), and then the same particles were vitrified for cryo-EM imaging (Figure S6D), with acquisition parameters summarized in

Table S4. After motion correction and CTF estimation, particles were extracted and subjected to iterative 2D classification (Figure S6E). High-quality classes were selected for 3D reconstruction using icosahedral symmetry, yielding a 3.24 Å map (Figures 6C and S6F) with local resolution reaching sub-4 Å across most of the capsid shell (Figure S6G). The atomic model of the asymmetric unit (ASU) was built, comprising four MCPs—three from a hexon and one from a penton (Figures 6D and 6E). Model statistics are provided in Table S4. The cryo-EM map and atomic model were deposited in the Electron Microscopy Data Bank and Protein Data Bank under IDs EMD-51699 and PDB: 9GYI, respectively.

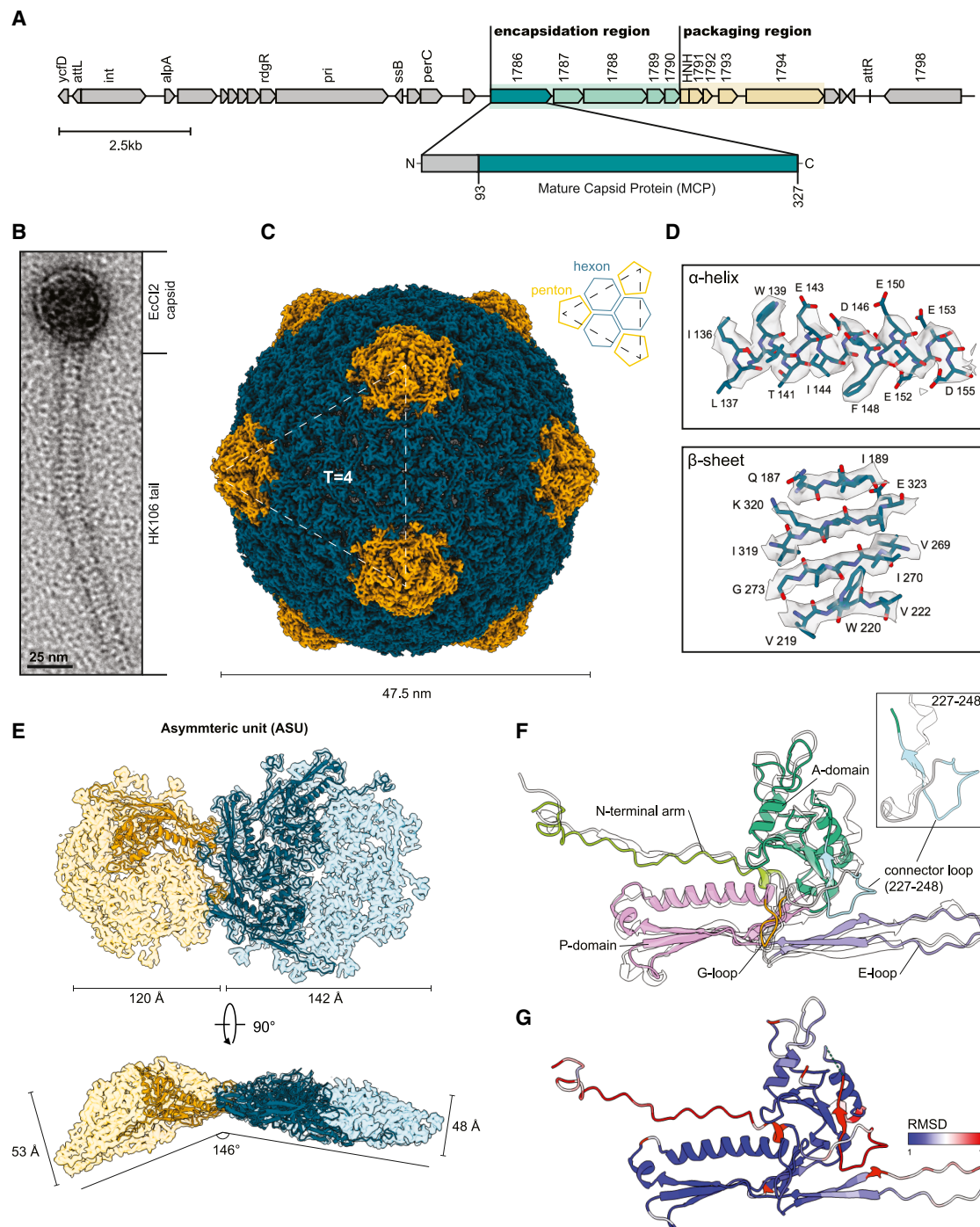


### Figure 6. Structure of the EcCl2 capsid

(A) Organization of the EcCl2 genome, highlighting the maturation of the protein product of gene 1786, yielding the 93–327 stretch of its mature major capsid protein (MCP).

(B) Negative-stain EM image of the infective particle of EcCl2, composed of the island-encoded capsid and the hijacked tail of the co-residing helper phage HK106. Scale bar represents 25 nm.

(C) 3.24 Å resolution map of the EcCl2 capsid with a diameter of 47.5 nm and T = 4 icosahedral symmetry. The capsid map is made up of 12 pentameric and 30 hexameric capsomers (pentons and hexons, shown in orange and teal, respectively).

(D) Side chain features of the atomic model (teal) and the corresponding map density section (gray) of a representative  $\alpha$  helix (top) and  $\beta$  sheet (bottom).

(E) The EcCl2 capsid map is made up of 60 asymmetric units (ASUs). Each comprises four neighboring MCP—one coming from a penton (orange) and three coming from an adjacent hexon (teal). The corresponding density maps of the entire penton (orange) and hexon (teal) are also shown to highlight differences

(legend continued on next page)



The assembled EcCl2 particle displays typical siphovirus morphology (Figure 6B), comprising a cf-PICI capsid and a long tail acquired from the co-residing HK106 phage. The capsid has a  $T = 4$  icosahedral symmetry and measures 47.5 nm in diameter (Figure 6C). This size closely resembles that of the classical (non-capsid-forming) PICI SaPI1 ( $T = 4$ , 50 nm; PDB: 6C22)<sup>28</sup> but is significantly smaller than the  $T = 7$  HK97 capsid (60 nm; PDB: 1OHG).<sup>29</sup> The compact EcCl2 capsid efficiently accommodates the 15.5 kbp genome of the island, with DNA arranged in concentric layers spaced  $\sim 23$  Å apart (Figure S6G). By contrast, the 41.5 kbp genome of HK106 (NCBI: NC\_019768) exceeds the internal volume of the EcCl2 capsid, providing a physical barrier to prevent helper phage propagation.

Topologically, the EcCl2 capsid comprises 240 MCPs arranged into 12 pentons (five MCPs each) and 30 hexons (six MCPs each) (Figure 6C). In nature, one penton is replaced by the portal complex, which serves as the DNA entry and tail attachment site. The mature MCP results from proteolytic cleavage, sharing the N-terminal motif (SxGxxAD) with HK97 (Figure S7A), suggesting a conserved maturation mechanism. The MCP adopts an HK97-like fold and overlays almost identically with HK97 (Figure 6F), with a root-mean-square deviation (RMSD) near 1 Å (Figure 6G). This fold includes canonical domains: N-terminal arm (N arm), glycine-rich loop (G loop), peripheral domain (P domain), extended loop (E loop), and axial domain (A domain) (Figure 6F).

A notable structural difference is the presence of a unique “connector loop” (residues 227–248) in EcCl2 MCP, bridging the G loop and A domain (Figures 6F and 6G). Though its functional role is uncertain, it resembles the S loop of phage P22 (Figure S7B),<sup>30</sup> which influences capsid size and symmetry.<sup>31,32</sup> We propose that the connector loop may serve a similar function, shifting symmetry from  $T = 7$  to  $T = 4$ , thus helping establish a structural barrier to helper phage interference.

Analysis of the four MCPs in the ASU revealed conformational differences, especially in the N arm, A domain, and E loop (Figure S7C). The penton MCP adopts a narrower conformation (N-arm to E-loop angle:  $146^\circ$ ), whereas hexon MCPs flatten progressively, reaching  $180^\circ$  in the broadest hexon MCP. These subtle differences translate into distinct capsomer shapes: pentons are narrower and taller ( $120$  Å  $\times$   $53$  Å), whereas hexons are wider and shorter ( $142$  Å  $\times$   $48$  Å) (Figure 6E).

### Interaction network between cf-PICI capsomers

In the  $T = 4$  icosahedral capsid of EcCl2, four distinct inter-capsomer interaction sites were identified and mapped onto a representative portion of the model (Figure 7A). Two sites occur at interfaces between adjacent pentons and hexons (Figures 7B

and 7C), while the other two are between adjacent hexons (Figures 7D and 7E). These interactions occur on two faces of the MCP: the N-arm face (Figures 7B and 7D) and the P-domain face (Figures 7C and 7E). N-arm face interactions occur along quasi-2-fold symmetry axes, where antiparallel N arms from adjacent capsomers, either penton-hexon (Figure 7B) or hexon-hexon (Figure 7D), interdigitate. By contrast, P-domain face interactions occur at quasi-3-fold axes, involving either penton-hexon-hexon (Figure 7C) or hexon-hexon-hexon (Figure 7E) assemblies. This 3-fold interaction network is common among phages with the HK97-like fold, such as R4C (PDB: 8GTA), TW1 (PDB: 5WK1), and RcGTA (PDB: 6TSU).<sup>33</sup> Each 3-fold vertex forms an extensive interaction network involving nine MCPs (three from each of three capsomers). These sites are organized into two layers: an inner layer comprising P domains, located near the center of the vertex, and an outer layer composed of E loops and N arms. This stratified architecture is clearly visualized in Figure 7E, where the nine MCPs are color coded by structural element and symmetry: P domains (teal), E loops (orange), and N arms (purple).

Detailed interactions within this network include multiple salt bridges (Figure 7F): between the P domain and E loop (K219-E151, Y175-N148, and E183-R156), between neighboring P domains (R345-D186), and between the N arm and E loop (D99-Q163). These interactions are stabilized by complementary electrostatic potentials: negatively charged grooves on the P-domain surface (Figure 7G) align with positively charged protrusions on the E loop (Figure 7H). A similar groove-protrusion electrostatic complementarity is observed in HK97 (Figure S7D; PDB: 1OHG).<sup>29</sup> However, unlike HK97, no covalent crosslinks between MCP subunits, such as the K169-N356 isopeptide bond characteristic of HK97 (Figure S7E) (PDB: 1OHG),<sup>29</sup> were detected in the EcCl2 capsid. This is corroborated by SDS-PAGE analysis, where EcCl2 MCPs migrated as monomers and no high-molecular-weight bands were observed (Figure S6B), in contrast to HK97 preparations.<sup>34</sup> These results suggest that the EcCl2 capsid is stabilized entirely by non-covalent interactions.

At the core of capsid assembly are the interactions between adjacent MCP subunits. In EcCl2, each MCP displays intrinsic polarity, with one positively charged face and one negatively charged face, promoting stable front-to-back assembly into capsomers (Figure 7I). This feature is also present in HK97 (Figure S7F; PDB: 1OHG).<sup>29</sup> Specific salt bridges between MCPs within pentons and hexons are detailed in Figures S8A and S8B, respectively.

### Structural validation of the cf-PICI capsid model

As described above, the EcCl2 MCP interaction network is entirely non-covalent, relying on a complex web of hydrogen

between the capsomers, with the penton being slightly narrower ( $120$  Å in width and  $53$  Å in height) than the hexon ( $142$  Å in width and  $48$  Å in height). Adjacent pentons and hexons are connected at a  $146^\circ$  angle.

(F) Structural representation of a single EcCl2 MCP with its topology resembling a typical HK97-like fold. The conserved domains are highlighted: N-terminal (N) arm (light green), glycine-rich (G) loop (orange), peripheral (P) domain (pink), extended (E) loop (purple), connector loop (blue), and axial (A) domain (green). The EcCl2 MCP is overlaid on the MCP of phage HK97 (PDB: 1OHG) (white cartoon), showing a nearly perfect match between the two structures, with the main divergence coming from the 227–248 connector loop.

(G) Root-mean-square deviation (RMSD) between the EcCl2 and HK97 MCP mapped onto the EcCl2 MCP, showing areas of low (blue) and high (red) structural difference between models.

See also Figures S6 and S7 and Table S4.

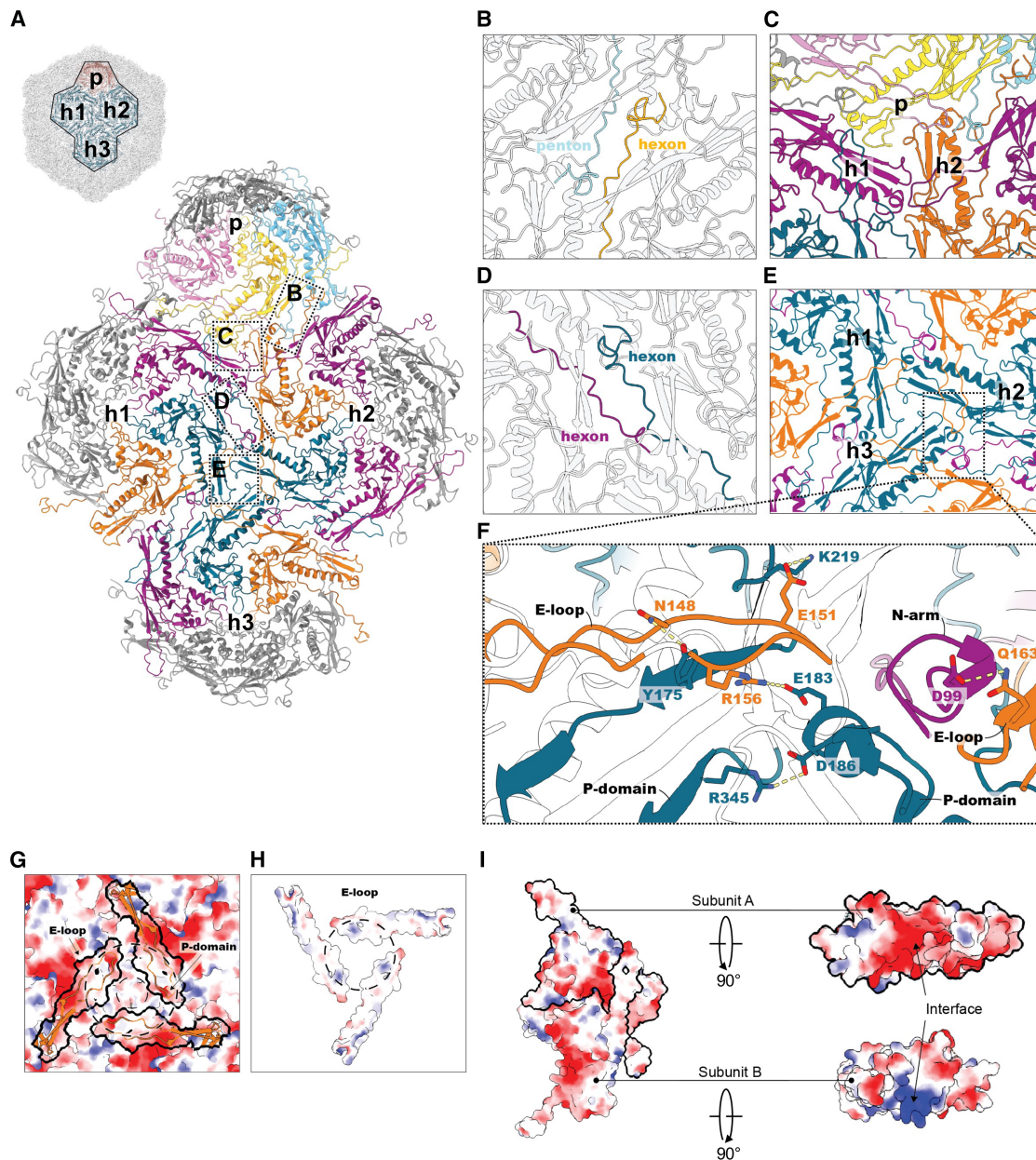


**Figure 7. Interaction details between EcCI2 capsomers and within them**

(A) Relative to the full capsid structure, there are four unique intercapsomere interaction sites (B–E) occurring between one penton (p) and three hexons (h1–h3). (B and C) Penton-hexon interactions are established by two anti-parallel N arms around a 2-fold axis (B) and between a pentamer and two hexamers around a 3-fold axis (C).

(D and E) Similarly, hexon-hexon interactions are formed around the 2-fold axis (D) and 3-fold axis (E).

(F) The detailed interaction network of the interface shown in (E). The five main interactions are established between three unique interaction sites: the P domain and E loop (K219 and E151, Y175 and N148, and E183 and R156), between two neighboring P domains (R345 and D186), and between the N arm and E loop (D99 and Q163). Salt bridges are marked with yellow dashed lines.

(G) Electrostatic surface potential of the interaction shown in (E) without the E loops, for which only the outlines and orange cartoons are shown.

(H) The electrostatic surface potential of the “bottom” side of the E loop. The dashed lines between (G) and (H) show an electrostatically complementary patch facilitating interaction.

(I) Electrostatic surface potential of two neighboring MCPs within a capsomer showing complementarity between the two interacting faces of subunits A and B. In electrostatic representations, the negative potential (red) corresponds to negatively charged residues, while positive potential (blue) indicates positively charged residues. Neutral regions are shown in white.

See also [Figures S7](#) and [S8](#).



bonds and salt bridges, with no contribution from decoration proteins. To validate our atomic model and identify critical residues for capsid assembly, we compared EcCI2 MCP interaction sites (Figures S8A and S8B) with those of the HK97 phage (PDB: 1OHG).<sup>29</sup> From this comparison, we selected residues with analogous positions in both structures that significantly influence local surface charge (Figures S8C and S8D).

In EcCI2 MCP, residues D257, K290, D295, and E319 were chosen alongside their counterparts in HK97 (D256, K289, R294, and R317, respectively). We also targeted EcCI2 residue R345, which plays a key role at the quasi-3-fold axis between neighboring hexons (Figures 7F and S8C), and the unique connector loop, deleting residues 232–247 within the original loop (residues 227–248) (Figures 6F and S8C). All mutations were designed to reverse the local charge (i.e., positive to negative or vice versa). We introduced the corresponding mutations into strains carrying either the HK97 prophage or the EcCI2 island, induced them by MC, and analyzed the formation of infectious particles. Overall, the EcCI2 capsid proved more sensitive to single-point mutations than HK97, highlighting the fragility of its non-covalent subunit interactions. Of the four HK97 mutations, two (K289D and D256K) reduced infectivity by 0.5 and 3 logs, respectively (Figure S8E). By contrast, all four corresponding EcCI2 mutations impaired transfer (Figure S8F): K290D and E319K completely abolished detectable transfer, while D295K and D257K reduced transfer by 2 and 4 logs, respectively. Additional EcCI2 mutants, R345D and the connector loop deletion, also abolished transfer, reinforcing their essential roles in capsid formation and/or stability (Figure S8F). This mutational analysis confirms the biological relevance of our EcCI2 capsid model and underscores the importance of electrostatic complementarity and fine-tuned non-covalent interactions for structural integrity and function. In comparison to HK97, the EcCI2 capsid displays a higher dependency on these interactions, reflecting its distinct architectural constraints.

## DISCUSSION

Since the discovery of cf-PICIs, a recurring question has been: what evolutionary advantage do these elements gain, compared with other satellites, by devoting part of their small genomes to a dedicated packaging module composed of nine genes? Other satellites typically encode only one or two genes for capsid formation and packaging.<sup>2</sup> Why would cf-PICIs prioritize packaging genes over auxiliary genes that might benefit their host and aid persistence? Here, we resolve this mystery.

Unlike classical satellites, which rely entirely on helper phages for both packaging and tail components, and thus the host tropism of these elements is already defined after their induction, cf-PICIs behave differently. First, they can produce packaged particles without phage induction, allowing their release in polysogenic clinical strains following prophage induction or phage infection. Second, cf-PICI capsids interact with tails from different species, enabling transfer within and between species. This tail promiscuity allows cf-PICIs to bypass extracellular barriers such as receptor changes,<sup>35</sup> capsules, or biofilms.<sup>36</sup> Third, their integration sites are conserved across and within species, ensuring successful integration. Finally, their transfer fre-

quencies exceed those of other satellites,<sup>37</sup> even without prophage induction, and across mixed-species bacterial populations. These features likely explain why cf-PICIs are the most prevalent satellites described to date.<sup>3</sup>

The phage tail serves as intricate nano-machinery, specifically designed to identify bacterial host cells, breach the cell wall and/or membrane, and inject the phage genome into the host cytosol, initiating the production of new viral particles.<sup>20</sup> Positioned at the distal end of the tail, the tail fibers (or spikes) facilitate the binding of the phage to specific receptors on the bacterial host surface, such as lipopolysaccharide (LPS), transmembrane proteins, teichoic acids, or even cellular organelles (e.g., pili or flagella).<sup>38,39</sup> These tail fibers (or spikes) predominantly dictate host specificity (or range) and influence the process of phage infection.<sup>20</sup> With a diverse array of phage tail fibers (or spikes),<sup>40</sup> phages effectively recognize and adhere to a wide spectrum of bacterial hosts. Notably, owing to their capacity to lyse bacterial cells, phages have emerged as potential therapeutic alternatives to antibiotics. However, their therapeutic potential is constrained by the fact that most phages infect only a limited range of strains due to the specific interaction between phage tail fibers and host receptors.<sup>41</sup> Moreover, bacteria can swiftly develop resistance by reducing the expression of the phage receptors or by blocking or masking these receptors through spontaneous mutation or phenotypic variation.<sup>42</sup> To overcome these limitations, there is growing interest in engineering characterized phages (primarily by manipulating tail fibers or spikes) to expand or reprogram their host range,<sup>43</sup> obviating the necessity for isolating new phages and adjusting phage cocktail compositions. Remarkably, cf-PICIs have effectively addressed all the aforementioned issues by generating cf-PICI capsids capable of interacting with various phage tails, thereby infecting different species and strains. Once again, our findings underscore PICIs as intriguing subcellular entities that have evolved unprecedented strategies to facilitate their dissemination in nature.

Traditionally, helper phages were defined as those inducing satellites and providing packaging components. We refine this concept by showing that induction, packaging, and particle formation need not rely on the same helper. Earlier studies used helpers that both induced the cf-PICI and provided tails.<sup>16</sup> Here, we show it is common for helpers to induce the island but not provide appropriate tails. Notably, cf-PICIs can package their DNA independently of helper phage induction but still require a separate phage for tail provision. This new scenario highlights the intricate and fascinating biology of cf-PICIs.

We also provide the first structural analysis of a capsid-forming PICI, EcCI2. Despite low sequence identity with phage HK97, EcCI2 assembles a nearly identical MCP, underscoring their evolutionary link. Like HK97, EcCI2 undergoes proteolytic maturation, preserving phage-like assembly mechanisms.

A key evolutionary adaptation observed in EcCI2 is its exclusive formation of smaller T = 4 capsids, in contrast to the T = 7 capsids of its helper HK106.<sup>16</sup> This size reduction, likely aided by terminase specificity, prevents accidental packaging of the helper genome and ensures selective cf-PICI DNA packaging.<sup>16,37</sup> A similar strategy is seen in non-capsid-forming PICIs like SaPI1, where morphogenesis proteins CpmA and

CpmB reduce capsid size.<sup>28</sup> Analogous strategies exist in other satellites, such as P4<sup>44</sup> or PLE.<sup>45</sup>

Structurally, EcCl2's capsid lacks decoration proteins, with the MCP alone forming the  $T = 4$  shell. A unique loop (residues 227–248) may act like the S loop in phage P22, altering symmetry and size. This supports a broader trend among PICIs to adapt capsid architecture for selective packaging. It may also reflect resource minimization ( $T = 4$  capsids require only 240 MCPs versus 420 for  $T = 7$ ), a potential advantage under stress.

On the molecular level, the evolution of cf-PICIs like EcCl2 is marked by their ability to exploit the structural versatility of the HK97 fold—a widely conserved organization regarded as “nature’s favorite building block” due to its capacity to form secure, shell-like entities of various sizes and symmetries.<sup>27,46</sup> This includes not only phage capsids (PDB: 1OHG),<sup>29</sup> but also bacterial and archaeal encapsulins (PDB: 3DKT and 2E0Z),<sup>47,48</sup> and now also cf-PICI. By forming smaller, tailless capsids, cf-PICIs have adapted this fold to create a unique packaging system that expands their host range and facilitates efficient gene transfer. This structural versatility is key to cf-PICIs’ evolution, enabling them to maintain distinct identities separate from their helper phages and avoid detrimental interactions that could hinder their propagation.

Unlike HK97, which uses covalent crosslinks between MCP subunits to stabilize its capsid, the EcCl2 capsid relies on a complex network of non-covalent interactions for stability while simultaneously maintaining the conserved fold needed for attachment of the tail. This highlights the complexity of structural trade-offs cf-PICIs must navigate, balancing mutations that enhance capsid stability while ensuring compatibility with the helper phage tail machinery. At the same time, cf-PICIs must remain distinct enough to avoid interference with the helper phage’s propagation. Overall, our structural data reveals the sophistication of cf-PICI as MGEs, shedding light on their evolutionary trajectory as specialized molecular pirates that play a significant role in shaping bacterial evolution and pathogenicity.

Cross-species particle formation is not unique to cf-PICIs. In co-infections with influenza A and respiratory syncytial virus (RSV), hybrid viral particles incorporating components from both viruses can form and broaden host tropism.<sup>49</sup> These structures, while infectious *in vitro*, remain to be confirmed in natural infections. Moreover, since cf-PICIs and their helpers share conserved assembly mechanisms,<sup>16</sup> it is tempting to speculate that phages might adopt similar strategies. However, most phage capsids are pre-tailed, making such events rare. Still, antiphage systems that block tail formation<sup>21</sup> may allow tailless phage capsids to be hijacked, favoring chimeric particle formation.

In summary, we reveal a new type of subcellular entity that packages specific DNA into non-infective particles, which become infective by acquiring tails from phages of other species. This ingenious strategy enables cf-PICIs to transfer DNA across species boundaries, representing a powerful evolutionary force in bacterial pathogens.

### Limitations of the study

While cf-PICIs are widespread and share common structural components for forming small-sized capsids, our study focused on cf-

PICIs from Proteobacteria, mainly *E. coli* and *K. pneumoniae*. Although capsid formation is essential, how different cf-PICI-encoded proteins specifically interact with their cognate partners, but not with phage-encoded ones, remains unknown. Another important area for future research is understanding why some cf-PICIs hijack tails from diverse phages while others are less promiscuous. Both the molecular basis and ecological consequences of these strategies require further study to fully grasp the impact of this gene transfer mechanism in nature.

### RESOURCE AVAILABILITY

#### Lead contact

Further information and requests for resources and reagents should be directed to and will be fulfilled by the lead contact, José R. Penadés ([j.penades@imperial.ac.uk](mailto:j.penades@imperial.ac.uk)).

#### Materials availability

Strains, phages, and plasmids generated in this study are available upon request and without restrictions from the [lead contact](#) upon request.

#### Data and code availability

The sequence of the mobilized cf-PICIs in different recipient strains can be found under BioProject accession PRJNA1214562. The cryo-EM density map of the EcCl2 capsid has been deposited at the Electron Microscopy Data Bank (EMDB) under accession code EMD-51699, and the associated atomic model has been deposited at the Protein Data Bank (PDB) under accession code 9GYI. All other data reported in this paper will be shared by the [lead contact](#) upon request. This paper does not report original code. Any additional information required to reanalyze the data reported in this paper is available from the [lead contact](#) upon request.

### ACKNOWLEDGMENTS

We would like to acknowledge Avinash Shenoy, Thomas Clarke, Patrice Nordmann, Vincent Perreten, Pilar Domingo-Calap, and Olaya Rendueles-Garcia for sharing their strains, phages, and/or plasmids. We would like to acknowledge Aravindan Illangovan for insights with the capsid model building, Joe Barritt for sharing his expertise of cryo-EM of phage capsids, Paul Simpson for the technical support, and Ambre Bexter for various insights on the first draft of the manuscript. Electron microscopy data acquisition was performed at the Centre for Structural Biology, Imperial College London. This work was supported by grants MR/X020223/1, MR/M003876/1, MR/V000772/1, and MR/S00940X/1 from the Medical Research Council (UK); BB/V002376/1 and BB/V009583/1 from the Biotechnology and Biological Sciences Research Council (BBSRC, UK); EP/X026671/1 from the Engineering and Physical Sciences Research Council (EPSRC, UK); and ERC-2023-SyG project 101118890—Talking Phages to J.R.P. and 215164/Z/18/Z/WT to T.R.D.C.

### AUTHOR CONTRIBUTIONS

L.H., J.B.P., T.R.D.C., and J.R.P. conceived the study; L.H., J.B.P., J.W., L.M.-R., C.H.S.A., and A.F.-S. conducted the experiments; L.H., J.B.P., J.W., L.M.-R., C.H.S.A., A.F.-S., T.R.D.C., and J.R.P. analyzed the data; T.R.D.C. and J.R.P. wrote the manuscript with input from L.H. and J.B.P.

### DECLARATION OF INTERESTS

Authors T.R.D.C. and J.R.P. filed a patent related to the research.

### STAR★METHODS

Detailed methods are provided in the online version of this paper and include the following:

- [KEY RESOURCES TABLE](#)

- **EXPERIMENTAL MODEL AND STUDY PARTICIPANT DETAILS**
  - Bacterial strains and growth conditions
- **METHOD DETAILS**
  - Plasmids and oligonucleotides
  - Phage and cf-PIC1 induction
  - Capsid precipitation and DNA extraction
  - Southern blotting
  - Densitometric analysis
  - cf-PIC1 transfer with exogenous tails
  - cf-PIC1 transfer with endogenous tails
  - Phage titration
  - DNA methods
  - cf-PIC1 transfer in mixed populations under different stresses
  - Co-cultivation and selection of KpCI1 transfer
  - Identification of cf-PIC1 candidates in virome samples
  - Whole genome sequencing
  - Bioinformatics analysis
  - EcCI2 purification
  - Grid preparation and cryo-EM data collection and processing
  - Atomic model building and refinement
  - Purification, negative-stain EM data collection and processing of tail-less KpCI1 and P1 phage
  - Purification and negative-stain EM of HK022 phage and free HK022 tails with KpCI1
- **QUANTIFICATION AND STATISTICAL ANALYSIS**

## SUPPLEMENTAL INFORMATION

Supplemental information can be found online at <https://doi.org/10.1016/j.cell.2025.08.019>.

Received: October 3, 2024

Revised: February 10, 2025

Accepted: August 13, 2025

## REFERENCES

1. Penadés, J.R., and Christie, G.E. (2015). The Phage-Inducible Chromosomal Islands: A Family of Highly Evolved Molecular Parasites. *Annu. Rev. Virol.* 2, 181–201. <https://doi.org/10.1146/annurev-virology-031413-085446>.
2. Penadés, J.R., Seed, K.D., Chen, J., Rocha, D.B., E.P.C., and Rocha, E.P.C. (2025). Genetics, ecology and evolutionary dynamics of phage satellites. *Nat. Rev. Microbiol.* 23, 410–422. <https://doi.org/10.1038/s41579-025-01156-z>.
3. de Sousa, J.A.M., Fillol-Salom, A., Penadés, J.R., and Rocha, E.P.C. (2023). Identification and characterization of thousands of bacteriophage satellites across bacteria. *Nucleic Acids Res.* 51, 2759–2777. <https://doi.org/10.1093/nar/gkad123>.
4. Chee, M.S.J., Serrano, E., Chiang, Y.N., Harling-Lee, J., Man, R., Bacigalupe, R., Fitzgerald, J.R., Penadés, J.R., and Chen, J. (2023). Dual pathogenicity island transfer by piggybacking lateral transduction. *Cell* 186, 3414–3426.e16. <https://doi.org/10.1016/j.cell.2023.07.001>.
5. Chen, J., Quiles-Puchalt, N., Chiang, Y.N., Bacigalupe, R., Fillol-Salom, A., Chee, M.S.J., Fitzgerald, J.R., and Penadés, J.R. (2018). Genome hypermobility by lateral transduction. *Science* 362, 207–212. <https://doi.org/10.1126/science.aat5867>.
6. Humphrey, S., Fillol-Salom, A., Quiles-Puchalt, N., Ibarra-Chávez, R., Haag, A.F., Chen, J., and Penadés, J.R. (2021). Bacterial chromosomal mobility via lateral transduction exceeds that of classical mobile genetic elements. *Nat. Commun.* 12, 6509. <https://doi.org/10.1038/s41467-021-26004-5>.
7. Chen, J., Ram, G., Penadés, J.R., Brown, S., and Novick, R.P. (2015). Pathogenicity island-directed transfer of unlinked chromosomal virulence genes. *Mol. Cell* 57, 138–149. <https://doi.org/10.1016/j.molcel.2014.11.011>.
8. Fillol-Salom, A., Rostøl, J.T., Ojiogu, A.D., Chen, J., Douce, G., Humphrey, S., and Penadés, J.R. (2022). Bacteriophages benefit from mobilizing pathogenicity islands encoding immune systems against competitors. *Cell* 185, 3248–3262.e20. <https://doi.org/10.1016/j.cell.2022.07.014>.
9. Frigols, B., Quiles-Puchalt, N., Mir-Sanchis, I., Donderis, J., Elena, S.F., Buckling, A., Novick, R.P., Marina, A., and Penadés, J.R. (2015). Virus Satellites Drive Viral Evolution and Ecology. *PLOS Genet.* 11, e1005609. <https://doi.org/10.1371/journal.pgen.1005609>.
10. Humphrey, S., San Millán, Á.S., Toll-Riera, M., Connolly, J., Flor-Duro, A., Chen, J., Ubeda, C., MacLean, R.C., and Penadés, J.R. (2021). Staphylococcal phages and pathogenicity islands drive plasmid evolution. *Nat. Commun.* 12, 5845. <https://doi.org/10.1038/s41467-021-26101-5>.
11. Fillol-Salom, A., Martínez-Rubio, R., Abdulrahman, R.F., Chen, J., Davies, R., and Penadés, J.R. (2018). Phage-inducible chromosomal islands are ubiquitous within the bacterial universe. *ISME J.* 12, 2114–2128. <https://doi.org/10.1038/s41396-018-0156-3>.
12. Martínez-Rubio, R., Quiles-Puchalt, N., Martí, M., Humphrey, S., Ram, G., Smyth, D., Chen, J., Novick, R.P., and Penadés, J.R. (2017). Phage-inducible islands in the Gram-positive cocci. *ISME J.* 11, 1029–1042. <https://doi.org/10.1038/ismej.2016.163>.
13. Six, E.W., and Klug, C.A.C. (1973). Bacteriophage P4: a satellite virus depending on a helper such as prophage P2. *Virology* 51, 327–344. [https://doi.org/10.1016/0042-6822\(73\)90432-7](https://doi.org/10.1016/0042-6822(73)90432-7).
14. O'Hara, B.J., Barth, Z.K., McKitterick, A.C., and Seed, K.D. (2017). A highly specific phage defense system is a conserved feature of the *Vibrio cholerae* mobilome. *PLOS Genet.* 13, e1006838. <https://doi.org/10.1371/journal.pgen.1006838>.
15. Barcia-Cruz, R., Goudenège, D., Moura de Sousa, J.A., Piel, D., Marbouty, M., Rocha, E.P.C., and Le Roux, F. (2024). Phage-inducible chromosomal minimalist islands (PICMIs), a novel family of small marine satellites of virulent phages. *Nat. Commun.* 15, 664. <https://doi.org/10.1038/s41467-024-44965-1>.
16. Alqurainy, N., Miguel-Romero, L., de Moura de Sousa, J.M., Chen, J., Rocha, E.P.C., Fillol-Salom, A., and Penadés, J.R. (2023). A widespread family of phage-inducible chromosomal islands only steals bacteriophage tails to spread in nature. *Cell Host Microbe* 31, 69–82.e5. <https://doi.org/10.1016/j.chom.2022.12.001>.
17. González-Gil, G., Bringmann, P., and Kahmann, R. (1996). FIS is a regulator of metabolism in *Escherichia coli*. *Mol. Microbiol.* 22, 21–29. <https://doi.org/10.1111/j.1365-2958.1996.tb02652.x>.
18. Christie, G.E., and Calendar, R. (2016). Bacteriophage P2. *Bacteriophage* 6, e1145782. <https://doi.org/10.1080/21597081.2016.1145782>.
19. Deeb, S.S. (1970). Studies on the In Vitro Assembly of Bacteriophage  $\phi$ 80 and  $\phi$ 80-Lambda Hybrids. *J. Virol.* 5, 27–31. <https://doi.org/10.1128/JVI.5.1.27-31.1970>.
20. Nobrega, F.L., Vlot, M., de de Jonge, P.A., Dreesens, L.L., Beaumont, H.J.E., Lavigne, R., Dutilh, B.E., and Brouns, S.J.J. (2018). Targeting mechanisms of tailed bacteriophages. *Nat. Rev. Microbiol.* 16, 760–773. <https://doi.org/10.1038/s41579-018-0070-8>.
21. He, L., Miguel-Romero, L., Patkowski, J.B., Alqurainy, N., Rocha, E.P.C., Costa, T.R.D., Fillol-Salom, A., and Penadés, J.R. (2024). Tail assembly interference is a common strategy in bacterial antiviral defenses. *Nat. Commun.* 15, 7539. <https://doi.org/10.1038/s41467-024-51915-4>.
22. Perna, N.T., Plunkett, G., Burland, V., Mau, B., Glasner, J.D., Rose, D.J., Mayhew, G.F., Evans, P.S., Gregor, J., Kirkpatrick, H.A., et al. (2001). Genome sequence of enterohaemorrhagic *Escherichia coli* O157:H7. *Nature* 409, 529–533. <https://doi.org/10.1038/35054089>.
23. Bel, S., Pendse, M., Wang, Y., Li, Y., Ruhn, K.A., Hassell, B., Leal, T., Winter, S.E., Xavier, R.J., and Hooper, L.V. (2017). Paneth cells secrete lysozyme via secretory autophagy during bacterial infection of the intestine. *Science* 357, 1047–1052. <https://doi.org/10.1126/science.aal4677>.

24. Tisza, M.J., and Buck, C.B. (2021). A catalog of tens of thousands of viruses from human metagenomes reveals hidden associations with chronic diseases. *Proc. Natl. Acad. Sci. USA* 118, e2023202118. <https://doi.org/10.1073/pnas.2023202118>.
25. Donà, V., Nordmann, P., Kittl, S., Schuller, S., Bouvier, M., Poirel, L., Endimiani, A., and Perreten, V. (2023). Emergence of OXA-48-producing *Enterobacter hormaechei* in a Swiss companion animal clinic and their genetic relationship to clinical human isolates. *J. Antimicrob. Chemother.* 78, 2950–2960. <https://doi.org/10.1093/jac/dkad337>.
26. Gertsman, I., Gan, L., Guttman, M., Lee, K., Speir, J.A., Duda, R.L., Hendrix, R.W., Komives, E.A., and Johnson, J.E. (2009). An unexpected twist in viral capsid maturation. *Nature* 458, 646–650. <https://doi.org/10.1038/nature07686>.
27. Duda, R.L., and Teschke, C.M. (2019). The amazing HK97 fold: versatile results of modest differences. *Curr. Opin. Virol.* 36, 9–16. <https://doi.org/10.1016/j.coviro.2019.02.001>.
28. Kizziah, J.L., Manning, K.A., Dearborn, A.D., Wall, E.A., Klenow, L., Hill, R.L., Spilman, M.S., Stagg, S.M., Christie, G.E., and Dokland, T. (2017). Cleavage and Structural Transitions during Maturation of *Staphylococcus aureus* Bacteriophage 80 $\alpha$  and SaPI1 Capsids. *Viruses* 9, 384. <https://doi.org/10.3390/v9120384>.
29. Helgstrand, C., Wikoff, W.R., Duda, R.L., Hendrix, R.W., Johnson, J.E., and Liljas, L. (2003). The refined structure of a protein catenane: the HK97 bacteriophage capsid at 3.44 Å resolution. *J. Mol. Biol.* 334, 885–899. <https://doi.org/10.1016/j.jmb.2003.09.035>.
30. Xiao, H., Zhou, J., Yang, F., Liu, Z., Song, J., Chen, W., Liu, H., and Cheng, L. (2023). Assembly and Capsid Expansion Mechanism of Bacteriophage P22 Revealed by High-Resolution Cryo-EM Structures. *Viruses* 15, 355. <https://doi.org/10.3390/v15020355>.
31. Rizzo, A.A., Suhanovsky, M.M., Baker, M.L., Fraser, L.C.R., Jones, L.M., Rempel, D.L., Gross, M.L., Chiu, W., Alexandrescu, A.T., and Teschke, C.M. (2014). Multiple Functional Roles of the Accessory I-Domain of Bacteriophage P22 Coat Protein Revealed by NMR Structure and CryoEM Modeling. *Structure* 22, 830–841. <https://doi.org/10.1016/j.str.2014.04.003>.
32. Suhanovsky, M.M., and Teschke, C.M. (2011). Bacteriophage P22 capsid size determination: Roles for the coat protein telokin-like domain and the scaffolding protein amino-terminus. *Virology* 417, 418–429. <https://doi.org/10.1016/j.virol.2011.06.025>.
33. Huang, Y., Sun, H., Wei, S., Cai, L., Liu, L., Jiang, Y., Xin, J., Chen, Z., Que, Y., Kong, Z., et al. (2023). Structure and proposed DNA delivery mechanism of a marine roseophage. *Nat. Commun.* 14, 3609. <https://doi.org/10.1038/s41467-023-39220-y>.
34. Gan, L., Conway, J.F., Firek, B.A., Cheng, N., Hendrix, R.W., Steven, A.C., Johnson, J.E., and Duda, R.L. (2004). Control of Crosslinking by Quaternary Structure Changes during Bacteriophage HK97 Maturation. *Mol. Cell* 14, 559–569. <https://doi.org/10.1016/j.molcel.2004.05.015>.
35. Samson, J.E., Magadán, A.H., Sabri, M., and Moineau, S. (2013). Revenge of the phages: defeating bacterial defences. *Nat. Rev. Microbiol.* 11, 675–687. <https://doi.org/10.1038/nrmicro3096>.
36. Haudiquet, M., Le Bris, J.L., Nucci, A., Bonnin, R.A., Domingo-Calap, P., Rocha, E.P.C., and Rendueles, O. (2024). Capsules and their traits shape phage susceptibility and plasmid conjugation efficiency. *Nat. Commun.* 15, 2032. <https://doi.org/10.1038/s41467-024-46147-5>.
37. Fillol-Salom, A., Bacarizo, J., Alqasbi, M., Ciges-Tomas, J.R., Martínez-Rubio, R., Roszak, A.W., Cogdell, R.J., Chen, J., Marina, A., and Penadés, J.R. (2019). Hijacking the Hijackers: *Escherichia coli* Pathogenicity Islands Redirect Helper Phage Packaging for Their Own Benefit. *Mol. Cell* 75, 1020–1030.e4. <https://doi.org/10.1016/j.molcel.2019.06.017>.
38. Bertozzi Silva, J.B., Storms, Z., and Sauvageau, D. (2016). Host receptors for bacteriophage adsorption. *FEMS Microbiol. Lett.* 363, fnw002. <https://doi.org/10.1093/femsle/fnw002>.
39. Dunne, M., Hupfeld, M., Klumpp, J., and Loessner, M.J. (2018). Molecular Basis of Bacterial Host Interactions by Gram-Positive Targeting Bacteriophages. *Viruses* 10, 397. <https://doi.org/10.3390/v10080397>.
40. Zinke, M., Schröder, G.F., and Lange, A. (2022). Major tail proteins of bacteriophages of the order Caudovirales. *J. Biol. Chem.* 298, 101472. <https://doi.org/10.1016/j.jbc.2021.101472>.
41. Gaborieau, B., Vaysset, H., Tesson, F., Charachon, I., Dib, N., Bernier, J., Dequidt, T., Georjon, H., Clermont, O., Hersen, P., et al. (2024). Prediction of strain level phage–host interactions across the *Escherichia* genus using only genomic information. *Nat. Microbiol.* 9, 2847–2861. <https://doi.org/10.1038/s41564-024-01832-5>.
42. Labrie, S.J., Samson, J.E., and Moineau, S. (2010). Bacteriophage resistance mechanisms. *Nat. Rev. Microbiol.* 8, 317–327. <https://doi.org/10.1038/nrmicro2315>.
43. Dunne, M., Prokhorov, N.S., Loessner, M.J., and Leiman, P.G. (2021). Reprogramming bacteriophage host range: design principles and strategies for engineering receptor binding proteins. *Curr. Opin. Biotechnol.* 68, 272–281. <https://doi.org/10.1016/j.copbio.2021.02.006>.
44. Agarwal, M., Arthur, M., Arbeit, R.D., and Goldstein, R. (1990). Regulation of icosahedral virion capsid size by the in vivo activity of a cloned gene product. *Proc. Natl. Acad. Sci. USA* 87, 2428–2432. <https://doi.org/10.1073/pnas.87.7.2428>.
45. Boyd, C.M., Subramanian, S., Dunham, D.T., Parent, K.N., and Seed, K.D. (2024). A *Vibrio cholerae* viral satellite maximizes its spread and inhibits phage by remodeling hijacked phage coat proteins into small capsids. *eLife* 12, RP87611. <https://doi.org/10.7554/eLife.87611>.
46. Suhanovsky, M.M., and Teschke, C.M. (2015). Nature's favorite building block: Deciphering folding and capsid assembly of proteins with the HK97-fold. *Virology* 479–480, 487–497. <https://doi.org/10.1016/j.virol.2015.02.055>.
47. Sutter, M., Boehringer, D., Gutmann, S., Günther, S., Prangishvili, D., Loessner, M.J., Stetter, K.O., Weber-Ban, E., and Ban, N. (2008). Structural basis of enzyme encapsulation into a bacterial nanocompartment. *Nat. Struct. Mol. Biol.* 15, 939–947. <https://doi.org/10.1038/nsmb.1473>.
48. Akita, F., Chong, K.T., Tanaka, H., Yamashita, E., Miyazaki, N., Nakaishi, Y., Suzuki, M., Namba, K., Ono, Y., Tsukihara, T., et al. (2007). The Crystal Structure of a Virus-like Particle from the Hyperthermophilic Archaeon *Pyrococcus furiosus* Provides Insight into the Evolution of Viruses. *J. Mol. Biol.* 368, 1469–1483. <https://doi.org/10.1016/j.jmb.2007.02.075>.
49. Haney, J., Vijayakrishnan, S., Streetley, J., Dee, K., Goldfarb, D.M., Clarke, M., Mullin, M., Carter, S.D., Bhella, D., and Murcia, P.R. (2022). Coinfection by influenza A virus and respiratory syncytial virus produces hybrid virus particles. *Nat. Microbiol.* 7, 1879–1890. <https://doi.org/10.1038/s41564-022-01242-5>.
50. Simossis, V.A., and Heringa, J. (2005). PRALINE: a multiple sequence alignment toolbox that integrates homology-extended and secondary structure information. *Nucleic Acids Res.* 33, W289–W294. <https://doi.org/10.1093/nar/gki390>.
51. Wishart, D.S., Han, S., Saha, S., Oler, E., Peters, H., Grant, J.R., Stothard, P., and Gautam, V. (2023). PHASTEST: faster than PHASTER, better than PHAST. *Nucleic Acids Res.* 51, W443–W450. <https://doi.org/10.1093/nar/gkad382>.
52. Gilchrist, C.L.M., and Chooi, Y.-H. (2021). clinker & clustermap.js: automatic generation of gene cluster comparison figures. *Bioinformatics* 37, 2473–2475. <https://doi.org/10.1093/bioinformatics/btab007>.
53. Ouyang, W., Mueller, F., Hjelmare, M., Lundberg, E., and Zimmer, C. (2019). ImJoy: an open-source computational platform for the deep learning era. *Nat. Methods* 16, 1199–1200. <https://doi.org/10.1038/s41592-019-0627-0>.
54. Punjani, A., Rubinstein, J.L., Fleet, D.J., and Brubaker, M.A. (2017). cryo-SPAR: algorithms for rapid unsupervised cryo-EM structure determination. *Nat. Methods* 14, 290–296. <https://doi.org/10.1038/nmeth.4169>.



55. Krissinel, E., and Henrick, K. (2007). Inference of macromolecular assemblies from crystalline state. *J. Mol. Biol.* 372, 774–797. <https://doi.org/10.1016/j.jmb.2007.05.022>.
56. Jamali, K., Käll, L., Zhang, R., Brown, A., Kimanius, D., and Scheres, S.H.W. (2024). Automated model building and protein identification in cryo-EM maps. *Nature* 628, 450–457. <https://doi.org/10.1038/s41586-024-07215-4>.
57. Emsley, P., Lohkamp, B., Scott, W.G., and Cowtan, K. (2010). Features and development of Coot. *Acta Crystallogr. D Biol. Crystallogr.* 66, 486–501. <https://doi.org/10.1107/S0907444910007493>.
58. Adams, P.D., Afonine, P.V., Bunkóczi, G., Chen, V.B., Davis, I.W., Echols, N., Headd, J.J., Hung, L.-W., Kapral, G.J., Grosse-Kunstleve, R.W., et al. (2010). PHENIX: a comprehensive Python-based system for macromolecular structure solution. *Acta Crystallogr. D Biol. Crystallogr.* 66, 213–221. <https://doi.org/10.1107/S0907444909052925>.
59. Chen, V.B., Arendall, W.B., Headd, J.J., Keedy, D.A., Immormino, R.M., Kapral, G.J., Murray, L.W., Richardson, J.S., and Richardson, D.C. (2010). MolProbity: all-atom structure validation for macromolecular crystallography. *Acta Crystallogr. D Biol. Crystallogr.* 66, 12–21. <https://doi.org/10.1107/S0907444909042073>.
60. Goddard, T.D., Huang, C.C., Meng, E.C., Pettersen, E.F., Couch, G.S., Morris, J.H., and Ferrin, T.E. (2018). UCSF ChimeraX: Meeting modern challenges in visualization and analysis. *Protein Sci.* 27, 14–25. <https://doi.org/10.1002/pro.3235>.
61. Gibson, D.G., Young, L., Chuang, R.-Y., Venter, J.C., Hutchison, C.A., and Smith, H.O. (2009). Enzymatic assembly of DNA molecules up to several hundred kilobases. *Nat. Methods* 6, 343–345. <https://doi.org/10.1038/nmeth.1318>.
62. Kaniga, K., Delor, I., and Cornelis, G.R. (1991). A wide-host-range suicide vector for improving reverse genetics in Gram-negative bacteria: inactivation of the *blaA* gene of *Yersinia enterocolitica*. *Gene* 109, 137–141. [https://doi.org/10.1016/0378-1119\(91\)90599-7](https://doi.org/10.1016/0378-1119(91)90599-7).
63. Ferrières, L., Hémerly, G., Nham, T., Guérout, A.-M., Mazel, D., Beloin, C., and Ghigo, J.-M. (2010). Silent Mischief: Bacteriophage Mu Insertions Contaminate Products of *Escherichia coli* Random Mutagenesis Performed Using Suicidal Transposon Delivery Plasmids Mobilized by Broad-Host-Range RP4 Conjugative Machinery. *J. Bacteriol.* 192, 6418–6427. <https://doi.org/10.1128/JB.00621-10>.
64. Datsenko, K.A., and Wanner, B.L. (2000). One-step inactivation of chromosomal genes in *Escherichia coli* K-12 using PCR products. *Proc. Natl. Acad. Sci. USA* 97, 6640–6645. <https://doi.org/10.1073/pnas.120163297>.

## STAR★METHODS

### KEY RESOURCES TABLE

REAGENT or RESOURCE	SOURCE	IDENTIFIER
<b>Antibodies</b>		
Ampicillin sodium salt	Merck (Sigma-Aldrich)	A9518; CAS 69-52-3
Kanamycin Sulfate	Merck (Sigma-Aldrich)	60615; CAS 70560-51-9
Chloramphenicol	Merck (Sigma-Aldrich)	C0378; CAS 56-75-7
Tetracycline	Merck (Sigma-Aldrich)	87128; CAS 60-54-8
Streptomycin sulfate	Merck (Sigma-Aldrich)	S6501-5G; CAS 3810-74-0
<b>Bacterial and virus strains</b>		
See Table S5 for bacterial strains	N/A	N/A
See Table S5 for bacteriophages	N/A	N/A
<b>Chemicals, peptides, and recombinant proteins</b>		
LB Broth (Lennox)	Merck (Sigma-Aldrich)	L3022
Bacteriological agar	VWR Chemicals	84609.05; CAS 9002-18-0
Nutrient Broth No. 2	Thermo Fisher Scientific (Thermo Scientific™)	10259632
Platinum® Taq DNA Polymerase High Fidelity	Thermo Fisher Scientific (Invitrogen™)	Cat# 11304011
DreamTaq DNA Polymerase	Thermo Fisher Scientific (Thermo Scientific™)	Cat# EP0703
KAPA HiFi plus dNTPs	Roche sequencing	7958846001
T4 DNA Ligase	Thermo Fisher Scientific (Invitrogen™)	10786591
GeneArt™ Gibson Assembly HiFi Master Mix	Thermo Fisher Scientific (Invitrogen™)	A46627
Mitomycin C	Merck (Sigma-Aldrich)	M0503; CAS 50-07-7
L-(+)-Arabinose	Merck (Sigma-Aldrich)	A3256; CAS 5328-37-0
Lysozyme	Merck (Sigma-Aldrich)	L6876-5G; CAS 12650-88-3
2,6-Diaminopimelic acid	Merck (Sigma-Aldrich)	33240-1G; CAS 583-93-7
Anhydrotetracycline hydrochloride	Merck (VETRANAL®)	37919; CAS 13803-65-1
Poly(ethylene glycol) 8000	Merck (Sigma-Aldrich)	89510-1KG-F; CAS 25322-68-3
Phenol:Chloroform:Isoamyl Alcohol 25:24:1, Saturated with 10mM Tris, pH 8.0, 1mM EDTA	Merck (Sigma-Aldrich)	P3803-100ML
Digoxigenin-11-dUTP	Merck (Roche)	11093088910
Anti-Digoxigenin-AP	Merck (Roche)	11093274910
CSPD	Merck (Roche)	11755633001
Blocking Reagent	Merck (Roche)	11096176001
DNA Molecular Weight Marker VII, DIG-labeled	Merck (Roche)	11669940910
Proteinase K	Merck (Sigma-Aldrich)	CAS 39450-01-6
Sucrose	Thermo Fisher Scientific (Invitrogen™)	10634932
Cesium Chloride	Merck (Sigma-Aldrich)	C4036
PEG 8,000	Thermo Fisher Scientific	418050100
Sodium Acetate trihydrate	Merck (Sigma-Aldrich)	S8625
DNAse I from bovine pancreas	Merck (Sigma-Aldrich)	DN25
RNAse A from bovine pancreas	Merck (Roche)	10109142001
Sodium Chloride	Merck (Sigma-Aldrich)	0000361439
Tris	Merck (Sigma-Aldrich)	252859

(Continued on next page)



## Continued

REAGENT or RESOURCE	SOURCE	IDENTIFIER
<b>Critical commercial assays</b>		
QIAquick PCR Purification Kit	QIAGEN	Cat# 28106
QIAprep Spin Miniprep Kit	QIAGEN	Cat# 27106
GenElute Bacterial Genomic DNA Kit	Merck (Sigma-Aldrich)	NA2110-1KT
<b>Deposited data</b>		
Atomic model of EcCl2 capsid	Protein Data Bank (PDB)	PDB: 9GYI
Cryo-EM map of EcCl2 capsid	Electron Microscopy Data Bank (EMDB)	EMDB: EMD-51699
Sequence of the mobilized cf-PICl in recipient strains	National Center for Biotechnology Information (NCBI)	NCBI: PRJNA1214562
<b>Oligonucleotides</b>		
See Table S6 for primers used in this study	N/A	N/A
<b>Recombinant DNA</b>		
See Table S6 for plasmids used in this study	N/A	N/A
<b>Software and algorithms</b>		
GraphPad prism10.3.0	N/A	<a href="https://www.graphpad.com/scientific-software/prism/">https://www.graphpad.com/scientific-software/prism/</a>
PRALINE multiple sequence alignment	Simossis et al. <sup>50</sup>	<a href="https://www.ibi.vu.nl/programs/pralinewww/">https://www.ibi.vu.nl/programs/pralinewww/</a>
SnapGene 7.1.2	N/A	<a href="https://www.snapgene.com/">https://www.snapgene.com/</a>
PHASTEST	Wishart et al. <sup>51</sup>	<a href="https://phastest.ca/">https://phastest.ca/</a>
Clinker	Gilchrist et al. <sup>52</sup>	<a href="https://cagecat.bioinformatics.nl/tools/clinker">https://cagecat.bioinformatics.nl/tools/clinker</a>
ImageJ	Ouyang et al. <sup>53</sup>	<a href="https://ij.imjoy.io/">https://ij.imjoy.io/</a>
Cryosparc 4.4.1	Punjani et al. <sup>54</sup>	N/A
PDBE Pisa 1.48	Krissinel et al. <sup>55</sup>	<a href="https://www.ebi.ac.uk/pdbe/pisa/picite.html">https://www.ebi.ac.uk/pdbe/pisa/picite.html</a>
ModelAngelo 1.0	Jamali et al. <sup>56</sup>	N/A
Coot 0.8.9	Emsley et al. <sup>57</sup>	N/A
Phenix 1.21	Adams et al. <sup>58</sup>	N/A
Molprobit 4.5.2	Chen et al. <sup>59</sup>	<a href="http://molprobit.biochem.duke.edu">http://molprobit.biochem.duke.edu</a>
UCSF ChimeraX 1.9	Goddard et al. <sup>60</sup>	<a href="https://www.cgl.ucsf.edu/chimerax/">https://www.cgl.ucsf.edu/chimerax/</a>
Galaxy version 0.7.19	N/A	<a href="https://usegalaxy.org/">https://usegalaxy.org/</a>
Adobe Illustrator 29.2.1	N/A	<a href="http://www.adobe.com">www.adobe.com</a>
Inkscape 1.3.2	N/A	<a href="https://inkscape.org/">https://inkscape.org/</a>
Bioicons	N/A	<a href="https://bioicons.com/">https://bioicons.com/</a>
<b>Other</b>		
Amicon® Ultra Centrifugal Filter, 30 kDaMWCO	Merck (Millipore)	UFC9030
Amicon® Ultra Centrifugal Filter, 100 kDaMWCO	Merck (Millipore)	UFC8100
1ml HiTrap Q XL column	Cytiva	17515801
R2/2 holey carbon film grids Cu 200	Quantifoil	Q66594
Fisherbrand™ Sterile PES Syringe Filter 0.2 µm	Fisher scientific	15206869

## EXPERIMENTAL MODEL AND STUDY PARTICIPANT DETAILS

### Bacterial strains and growth conditions

Phages and bacterial strains used in this study are listed in Table S5. *E. coli*, *K. pneumoniae*, *E. hormaechei*, *Enterobacter cloacae*, *Citrobacter koseri*, *Citrobacter freundii* and *Salmonella enterica* strains were grown at 37°C or 30°C on Luria-Bertani (LB) agar or in LB

broth with shaking (120 r.p.m.). When appropriate, Ampicillin (100 µg/mL), Streptomycin (100 µg/mL), Kanamycin (30 µg/mL), Tetracycline (20 µg/mL), or Chloramphenicol (20 µg/mL) were added. For auxotrophic *E. coli* strain S17 MFD<sub>pir</sub>, 0.3 mM DAP (2,6-Diaminopimelic acid, Sigma-Aldrich) was added when required.

## METHOD DETAILS

### Plasmids and oligonucleotides

The plasmids and oligonucleotides used in this study are listed in [Table S6](#). The plasmid pWRG99-*kmR* for mutagenesis was constructed using Gibson assembly,<sup>61</sup> using the oligonucleotides referenced in [Table S6](#). Additional plasmids were generated by cloning PCR products (amplified with oligonucleotides from [Table S6](#)) into the pBAD18 or pKNG101 vector via restriction-ligation. All plasmids were verified by Sanger sequencing in Eurofins Genomics.

### Phage and cf-PICI induction

Overnight cultures of lysogenic strains were diluted in 1:50 in LB and then sub-cultured until OD<sub>600</sub> = 0.15. Mitomycin C was added at the final concentration of 2 µg/mL. The sub-cultures were supplemented with 0.02% L-arabinose only if the strains contained pBAD18 derivative plasmids to express corresponding proteins. Sub-cultures were subsequently incubated at 80 r.p.m. at 30 °C for 4 hours followed by incubating at 25 °C without shaking overnight. Following induction, lysates were collected, centrifuged and then filtered using sterile 0.2 µm filters. The number of phage particles in the lysates was quantified.

### Capsid precipitation and DNA extraction

Following phage and cf-PICI induction, 35 mL lysates were filtered through 0.2 µm sterile filters and treated with DNase and RNase. Capsids were precipitated using PEG 8000 (Polyethylene Glycol 8000, Sigma-Aldrich) after centrifugation at 11,000 g, and then re-suspended in 200 µL Phage Buffer (PHB, 50 mM Tris pH 8.0, 1 mM NaCl, 1mM MgSO<sub>4</sub>, 4mM CaCl<sub>2</sub>). The precipitated lysates were lysed in 200 µL Lysis Mix (9.5 µL SDS 20%, 4.5 µL 20 mg/mL proteinase K, 90 µL H<sub>2</sub>O) at 55 °C for 1 hour. DNA was extracted with Phenol:Chloroform:Isoamyl Alcohol method and resuspended in 50 µL TE buffer (pH 8.0). 0.4 µL DNA was used for electrophoresis analysis, followed by Southern blotting analysis.

### Southern blotting

After phage and cf-PICI induction, 1.5 mL samples were taken at defined time points and pelleted. DNA was extracted using the bacterial genomic DNA kit (GenElute Bacterial Genomic DNA Kit, Sigma-Aldrich). 5 µL genomic DNA was separated in a 0.7% agarose gel at 25V overnight, treated with 0.25 M HCl and 0.4 M NaOH, and transferred to a nylon membrane (Nylon Membranes positively charged, Roche) by inverse capillarity. The membrane was hybridized with a DIG-labeled probe (Digoxigenin-11-dUTP, alkali-stable; Roche), washed, and detected using an anti-DIG antibody (Anti-Digoxigenin-AP; Roche) and CSPD (Roche). Primers used for DIG-labeled probes are listed in [Table S6](#).

### Densitometric analysis

Densitometric analyses to compare DNA bands in agarose gels or Southern blot assays were performed with ImageJ.<sup>53</sup> Images were converted to 8-bits by linearly scaling from min-max to 0–255 and the mean grayscale values of the detected area of the same size were measured. Lower grayscale values correspond to higher DNA amounts.

### cf-PICI transfer with exogenous tails

To measure cf-PICI transfer, a tetracycline resistance cassette (*tetA*) was inserted into EcCI1 and KpCI1, while a chloramphenicol resistance cassette (*cat*) was inserted into EcCI2.

50 µL of cf-PICI lysate and 50 µL of phage WT or mutant lysate were mixed and incubated at 25 °C for 30 mins, followed by a 10-fold serial dilution in PHB. 100 µL of diluted lysate was added to 1 mL recipient strain (OD<sub>600</sub> = 1.4 for *E. coli*, OD<sub>600</sub> = 0.6 for *K. pneumoniae*, *E. hormaechei*, *Enterobacter cloacae*, *Citrobacter koseri*, *Citrobacter freundii* and *Salmonella enterica*) supplemented with 4.4 mM CaCl<sub>2</sub>, following by incubation at 37 °C for 30 mins. 3 mL LB top agar (LTA, 20 g of LB Broth, Sigma-Aldrich; 7.5g agar) were then added to the samples and plated on the LBA plate with selective antibiotics (20 µg/mL tetracycline for EcCI1 and KpCI1; 20 µg/mL chloramphenicol for EcCI2). The plates were incubated at 37 °C for 48 hours. The number of forming colonies was counted and represented as CFU/mL of cf-PICI lysate. PCR was used to verify cf-PICI integration in recipient strains. Primers used for PCR are listed in [Table S6](#). Mobilized KpCI1 in C1a (strains JP24826, JP25920 and JP25921), in GN02175 ΔEcCI1 (strains JP25235, JP25925 and JP25926), in EDL933 (strains JP25631, JP25921 and JP25922) and in RHBSTW-00139 (strains JP25633, JP25923 and JP25924), and mobilized EcCI1 in Eh<sub>h</sub>\_18 ΔEh<sub>h</sub>CI<sub>h</sub>\_18 (strains JP25149, JP25927 and JP25928) were also verified by Nanopore long-read sequencing (Bioproject: PRJNA1214562) in Plasmidsaurus.

To maximize the detection of cf-PICI transfer and measure the transfer of the same cf-PICI with different WT *E. coli* phages comparably, these *E. coli* phages (HK022 and HK106) were quantified to PFU/mL = 10<sup>10</sup>. The same procedure was followed as above. Colony counts were represented as CFU/mL of cf-PICI lysate.

### cf-PICl transfer with endogenous tails

A 10-fold serial dilution of cf-PICl lysate using PHB was performed. 100  $\mu$ L of diluted lysate was added to 1 mL recipient strain ( $OD_{600} = 1.4$  for *E. coli*, and  $OD_{600} = 0.6$  for *E. hormaechei*) supplemented with 4.4 mM  $CaCl_2$ , and incubated at 37 °C for 30 mins. 3 mL LTA were then added to the sample and plated on the LBA plate with selective antibiotics. The plates were incubated at 37 °C for 48 hours. The number of forming colonies was counted and represented as CFU/mL of cf-PICl lysate.

### Phage titration

Recipient strains were sub-cultured until  $OD_{600} = 0.34$ . Bacterial lawns were prepared by mixing 300  $\mu$ L of cells with phage top agar (PTA; 25 g of Nutrient Broth No. 2, Oxoid; 4g agar) and poured onto square plates with phage bottom agar (PBA; 25 g of Nutrient Broth No. 2, Oxoid; 7g agar) supplemented with 10 mM  $CaCl_2$ . Serially diluted phage lysates were spotted on the agar. Plates were incubated at 37°C for 24 hours. Plaques were counted and quantified as plaque-forming units (PFU/mL).

For HK97 capsid mutagenesis verification experiments, PBA was supplemented with 0.02% L-arabinose to induce the expression of WT HK97 capsid in recipient strains.

### DNA methods

For phage and cf-PICl scarless deletion, an allelic replacement method was performed. Empty attachment sites of bacteria (*attB*) along with their flanking regions were amplified by PCR using primers listed in Table S6 and then cloned to the allelic-exchange vector pKNG101.<sup>62</sup> The constructed pKNG101 derivatives were trans-conjugated from the auxotrophic donor strain S17 MFD<sub>pir</sub> to the recipient strain.<sup>63</sup> Overnight cultures of donor and recipient strains were washed with PBS, mixed at a 1:1 ratio, and spotted on LBA plates with DAP for conjugation at 37°C. Transconjugants were selected on LBA plates with 100  $\mu$ g/mL streptomycin. Sucrose-sensitive transconjugants were cultured in LB without NaCl at 30 °C overnight. The second recombination event was selected on NaCl-free LBA plates complemented with 20% sucrose at 37°C. Mutants obtained were verified by PCR and Sanger sequencing in Eurofins Genomics.

The HK022 tail deletion mutant was constructed based on the allelic-exchange vector pKNG101. The flanking regions of the HK022 major tail gene were amplified using primers from Table S6 and cloned into pKNG101. The remaining gene mutagenesis process was performed as above described. Mutants were verified by PCR and Sanger sequencing in Eurofins Genomics.

Gene insertions or deletions in *E. coli* and *K. pneumoniae* were performed using a  $\lambda$  Red recombinase-mediated method.<sup>64</sup> The kanamycin resistance cassette (*kmR*) or tetracycline resistance cassette (*tetA*) was amplified from pKD4 or JP9802 by PCR using primers listed in Table S6. In brief, PCR products were electroporated into the recipient strains harboring pWRG99 or pWRG99-*kmR*, allowing  $\lambda$  Red recombinase-mediated insertion of antibiotic cassettes into the bacterial genome. To remove *kmR* cassette flanked by flippase recognition target (*FRT*) sites, a thermal sensitive plasmid pCP20 was transformed into the corresponding strain. The strains carrying pCP20 were cultured at 30 °C overnight with ampicillin to permit FLP recombination. Overnight culture was diluted in fresh ampicillin-free LB at a 1:50 ratio and then grown at 42 °C for 5 h to promote plasmid loss. Kanamycin-sensitive colonies were selected and verified by PCR and Sanger sequencing in Eurofins Genomics.

For deletion of  $\beta$ -Lactamase gene *shv-1* from DSM30104, the *tetA* cassette was first inserted to replace *shv-1* using pWRG99-*kmR*. The *tetA* cassette was then replaced by a *kmR* cassette flanked by *FRT* sites, followed by the deletion of *kmR* using pCP20. Mutants were verified by PCR and Sanger sequencing in Eurofins Genomics.

Site-directed scarless mutagenesis of KpC11 *alpA* and EcC12 *capsid* mutants was performed as previously described.<sup>37</sup> The *kmR* cassette flanked by I-SceI recognition sites was PCR-amplified from pWRG717 using primers listed in Table S6. PCR products were then electroporated into the recipient strains harbouring pWRG99 for  $\lambda$  Red recombinase-mediated insertion. Mutants with inserted cassettes were verified by PCR. After that, a second PCR product containing the desired mutations were electroporated into the strain with cassette. The second recombination event was selected on LBA plates with anhydrotetracycline (AHT)-induced I-SceI meganuclease at 30 °C. Mutants were verified by PCR and Sanger sequencing in Eurofins Genomics.

### cf-PICl transfer in mixed populations under different stresses

Non-lysogenic *K. pneumoniae* JP24871 carrying KpC11 was sub-cultured 1:50 in fresh LB without antibiotics until  $OD_{600} = 0.2$ . The strain was then treated overnight with no treatment (control), lytic phage K68 QB (MOI = 0.01), fresh lysozyme (500  $\mu$ g/mL), or ampicillin (50  $\mu$ g/mL) at 80 r.p.m. at 30 °C for 4 h followed by incubating at 25 °C without shaking overnight. Filtered lysates were tested for transfer in *E. coli* C1a, using exogenous phage HK022. The number of forming colonies was counted and represented as CFU/mL of cf-PICl lysate.

### Co-cultivation and selection of KpC11 transfer

Single colony of *E. coli* recipient strain, *E. coli* lysogen strain and *K. pneumoniae* strain (containing KpC11  $\Delta$ orf17::tetA) was inoculated in LB with appropriate antibiotics for overnight, respectively. The overnight culture was centrifuged at 4200 r.p.m. and then the supernatant was discarded to eliminate the antibiotics. The pellet was resuspended by LB without antibiotics. This resuspended overnight culture was diluted in 1:50 in LB without antibiotics and then sub-cultured at 120 r.p.m. at 37 °C until  $OD_{600} = 0.2$ . The sub-cultures of *E. coli* and *K. pneumoniae* were mixed at the ratio 1:1:1 followed by co-cultured at 80 r.p.m. at 30 °C for 5 hours. After that, 1 mL co-culture was added 3 mL LTA and plated on LBA plated containing both 30  $\mu$ g/mL kanamycin and 20  $\mu$ g/mL tetracycline to

select the transferred KpCI1 from *K. pneumoniae* to *E. coli*. Number of forming colonies was counted and represented as colony forming units (CFU/mL of co-culture).

### Identification of cf-PICI candidates in virome samples

We searched for cf-PICIs in metagenome studies, focusing on their common features as previously described.<sup>11,12,16</sup> Specifically, we targeted cf-PICIs with: (i) a size of approximately 10–18 kb; (ii) conserved gene organization, including an integration module, along with a regulation module, replication module, and exclusive packaging modules (capsid, protease, portal, adaptor, connector, HNH endonuclease, small terminase, large terminase); and (iii) the absence of lytic genes and a complete tail module.

### Whole genome sequencing

Whole genome sequencing of capsid DNA was conducted by SeqCenter using the Illumina NextSeq 2000 platform, generating  $2 \times 151$  bp paired-end reads. The resulting reads were aligned to the reference genome using Map with BWA-MEM (Galaxy version 0.7.19), and coverage of the reads across genomic contigs was visualized using BAM Coverage Plotter (Galaxy version 20201223+galaxy0).

Whole genome sequencing of mobilized cf-PICIs in various recipient strains was performed by Plasmidsaurus employing Oxford Nanopore long-read sequencing technology. Libraries were prepared without amplification using the latest v14 library preparation chemistry, which enables minimal fragmentation of genomic DNA in a sequence-independent manner, thereby facilitating high-quality genome assembly. Mobilized cf-PICIs in various recipient strains was deposited in the NCBI database under Bioproject PRJNA1214562.

### Bioinformatics analysis

Prophages in natural isolated were predicted by PHASTEST.<sup>51</sup> Comparison of phage or cf-PICI sequences was based on BLASTn, BLASTp, Clinker<sup>52</sup> and PRALINE alignments.<sup>50</sup>

### EcCI2 purification

The *E. coli* strain JP24598, which overexpresses *alpA* to promote EcCI2 reproduction,<sup>16</sup> was grown overnight at 37°C in LB medium supplemented with 100 µg/mL of ampicillin with 180 rpm shaking. On the next day, 1 mL of the overnight culture was added into each of 3x1L of fresh LB supplemented with 100 µg/mL ampicillin and grown at 37°C, 180 rpm until OD<sub>600</sub>=0.05. 0.02% L-arabinose was added, and growth was continued at 37°C, 120 rpm until OD<sub>600</sub>=0.1–0.2. Phage was induced by addition of 2 µg/mL MC and incubated for 4 h at 32°C, 80 rpm. The cultures were further incubated overnight at room temperature (RT) for bacterial complete lysis. On the next day, 0.2 mg/mL lysozyme, 1 µg/mL RNase and 1 µg/mL DNase I was added to the lysates and incubated for 1 h at RT. The cultures were centrifuged at 10,000 x G for 20 min at 4°C to remove cell debris, and the supernatant was collected and spun down again at 10,000 x G for 20 min at 4°C. The supernatant was transferred into a beaker and 1M NaCl was added, followed by 1 h incubation at 4°C with gentle stirring. After the lysate was centrifuged at 10,000 x G for 20 min at 4°C, the supernatant was supplemented with 10% PEG 8,000 and stirred until dissolved. The solution was then incubated without stirring overnight at 4°C. On the next day, the precipitate was collected by centrifugation at 10,000 x G for 30 min at 4°C and the remaining liquid was removed by placing the tube upside down for 30 min. All pellets were resuspended by addition of 3 mL phage buffer (50mM Tris, pH=8, 100 mM NaCl, 1 mM MgSO<sub>4</sub>) and gently pipetting up and down. The resulting resuspension was applied on top of a pre-layered 1.3, 1.4 and 1.6 g/cm<sup>3</sup> CsCl density gradient. After 2 h ultracentrifugation at 80,000 x G at 4°C, the visible EcCI2 containing layer was collected and dialysed overnight against dialysis buffer (50mM Tris, pH 8.4, 100 mM NaAc). Following dialysis, the EcCI2 sample was slowly diluted with 50 mL of buffer A (50 mM Tris, pH 8.4, 10 mM NaAc) and loaded into a 1 mL Q Column XL (Cytvia) pre-equilibrated with buffer A. The column was extensively washed with buffer A, followed by a gradient elution with buffer B (50 mM Tris pH 8.4 2M NaAc) over 80 mL. Free helper phage tails were eluted at 300–500 mM NaAc, and the assembled EcCI2 particles at 800 mM to 1M NaAc. The eluted particles were dialysed against buffer A and gently concentrated using a 30,000 MWCO centrifugal concentrator (Amicon). For storage, particles were filtered through a 0.2 µm filter and kept at 4°C. The determined EcCI2 titer in the sample was approximately  $3 \times 10^{10}$  particles.

### Grid preparation and cryo-EM data collection and processing

3 µl of freshly prepared EcCI2 sample was applied on glow discharged (70s) holey carbon Quantifoil R2/2 200 mesh grids (Agar Scientific) using Vitrobot (Thermo) operating at 95% humidity at 4°C and vitrified in liquid ethane. The cryo-EM data was acquired using a Glacios Microscope (Thermo Scientific), operating at 200kV and equipped with Falcon 4 direct electron detector. 4337 movies were recorded using EPU software at a magnification of x100000, corresponding to 1.1 Å/px pixel size, 50 e<sup>−</sup>/Å<sup>2</sup> electron dose and a defocus range of −0.8 to −2.8 µm. All processing was performed within CryoSPARC v4.4.1 software.<sup>54</sup> After all movies were motion- and CTF-corrected, the micrographs were curated to select those with ideal ice thickness, CTF estimation and resolution. From a total of 3525 selected micrographs, 200 capsid particles were manually picked and 2D classified to generate templates for automated particle picking in the entire dataset. A total of 4658 particles were automatically picked and extracted after binning to a box size of 1000 px. Low quality particles were removed after several rounds of 2D classification, followed by a final extraction with a larger box size of 1300 px and subsequent downsampling by Fourier cropping to 500 px. Following a final round of 2D classification, 1933 particles

were selected to generate an ab initio model that was non-uniform refined to an estimated 3.24 Å resolution when an icosahedral symmetry was imposed. The local resolution of the final map was estimated in CryoSPARC and visualised in ChimeraX.<sup>60</sup> Details of the data collection and 3D refinement are provided in Table S4.

### Atomic model building and refinement

The initial atomic model of the ASU was built using ModelAngelo,<sup>56</sup> followed by manual correction of chain placements and real-space refinement in Coot.<sup>57</sup> The resulting model was refined iteratively with Phenix<sup>58</sup> until Ramachandran outliers and poor rotamers were in the favored regions. The final atomic model was validated with MolProbity<sup>59</sup> and Phenix<sup>58</sup> and visualized in ChimeraX.<sup>60</sup> Contacts between chains were detected using ChimeraX<sup>60</sup> and PDBe PISA software<sup>55</sup> (<https://www.ebi.ac.uk/pdbe/pisa/picite.html>). The final capsid map and model was deposited under EMD-51699 and PDB ID 9GYI.

### Purification, negative-stain EM data collection and processing of tail-less KpCI1 and P1 phage

Tail-less KpCI1 were obtained from strains DSM30104 and JP24891; phage P1 from strain JP24467 and all three were purified in the same way. In short, following induction with 2 µg/mL MC and incubation for 4 h at 32°C, 80 rpm, cultures were further incubated overnight at RT for complete lysis. On the next day, 0.2 mg/mL lysozyme, 1 µg/mL RNase and 1 µg/mL DNase I was added to the lysates and incubated for 1 h at RT. The cultures were centrifuged at 11,000 x G for 20 min at 4°C to remove cell debris, and the supernatant was precipitated with 1M NaCl and 10% PEG 8,000 overnight at 4°C. On the next day, the precipitate was collected by centrifugation at 11000 x G for 10 min at 4°C, and was resuspended with phage buffer (50mM Tris, pH=8, 100 mM NaCl, 1 mM MgSO<sub>4</sub>). The resuspended solution was treated with 50% chloroform and mildly vortexed for 5 s to further remove cell debris. After centrifugation at 11,000 x G for 5 min at 4°C, the upper phase was collected and KpCI1/P1 particles were then concentrated using a 100,000 MWCO centrifugal concentrator to ~30 µl. Purified samples were directly applied onto glow-discharged carbon coated copper grids (300 mesh, Agar Scientific) and incubated for 1 min at RT. Grids were washed three times in 10 µl of phage buffer, excess was blotted away with filter paper and the grids were stained for 30 s with 1% phosphotungstic acid (pH=7.0). Negative-stain EM images were acquired using FEI Tecnai 12 Spirit operating at 120 kV equipped with a LaB6 filament and a CCD TVIPS fast frame camera. Three separate negative-stain EM datasets have been collected, comprising 200, 26 and 98 micrographs at pixel size of 3.6, 7.295, and 3.6 Å/px for DSM30104, JP24467 and JP24891 samples, respectively. Micrographs were processed using CryoSPARC, where KpCI1 and P1 particles were automatically picked, extracted and underwent a 2D classification process which isolated well-defined 2D class averages containing a total of 99, 79 and 56 particles of KpCI1 (DSM30104), P1 (JP24467) and KpCI1 (JP24891), respectively. The diameter measurements were done in ImageJ.

### Purification and negative-stain EM of HK022 phage and free HK022 tails with KpCI1

HK022 virions and HK022 free tails were purified using JP24850 and JP25009 strains, respectively, following a similar procedure as described above for KpCI1 and P1 particles with some additional steps. In short, following precipitation, the resulting pellet was applied onto a pre-layered 1.3, 1.4 and 1.6 g/cm<sup>3</sup> CsCl density gradient. After 2h ultracentrifugation at 80,000 x G at 4°C, the layer containing a visible band was collected and HK022 virions were dialysed against phage buffer and used for negative-stain EM right after. The HK022 free tails were dialysed against buffer C (50mM Tris 8.4 50mM NaCl) and loaded into a 1 mL Q Column XL (Cytiva) pre-equilibrated with buffer C. The column was extensively washed with buffer C, followed by a gradient elution with buffer D (50 mM Tris pH 8.4 1M NaCl) over 35 ml. Fractions corresponding to the dominant peak were pooled, dialysed against phage buffer after which 10 µl of purified HK022 tails were combined with 10 µl of purified tail-less KpCI1, incubated for 30min at 37°C, and used directly for negative-stain EM.

10µl Samples of HK022 as well as KpCI1 with HK022 tails were directly applied onto glow-discharged carbon coated copper grids (300 mesh, Agar Scientific) and incubated for 2 min at RT. Grids were washed three times in 10 µl of phage buffer, excess was blotted away with filter paper and the grids stained for 60 s with 0.2% uranyl acetate. Negative-stain EM images were acquired using FEI Tecnai 12 Spirit operating at 120 kV equipped with a LaB6 filament and a CCD TVIPS fast frame camera.

### QUANTIFICATION AND STATISTICAL ANALYSIS

Experiments were repeated four times, with sample sizes indicated in the figure legends. Data are presented as mean ± SD. Statistical analyses were performed with GraphPad Prism v.10. One-way ANOVA with Dunnett's multiple comparisons test or Two-way ANOVA with Sidak's multiple comparisons test was performed to compare three or more groups. An unpaired t-test was applied to compare two groups. Adjusted P values as: ns: P > 0.05; \*: P ≤ 0.05; \*\*: P ≤ 0.01; \*\*\*: P ≤ 0.001; \*\*\*\*: P ≤ 0.0001.



# Supplemental figures

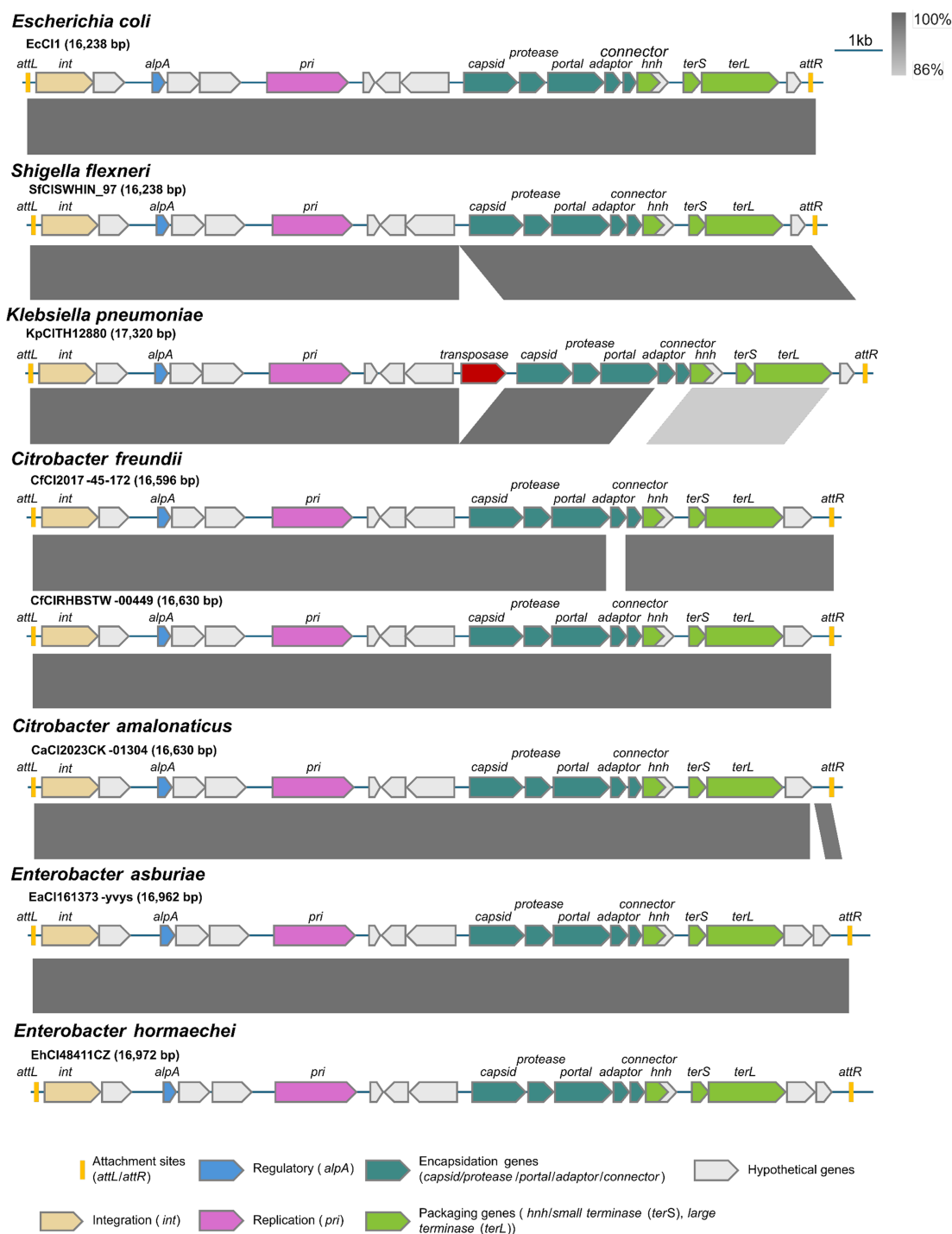


**Figure S1. EcCl1 is present in five different bacterial genera and seven different bacterial species, related to Figure 1**  
Genes are colored according to their sequence and function. Gray arrows indicate hypothetical proteins. Gray scales between cf-ICl sequences indicate that the regions share similarity, based on BLASTn. See also Table S1.



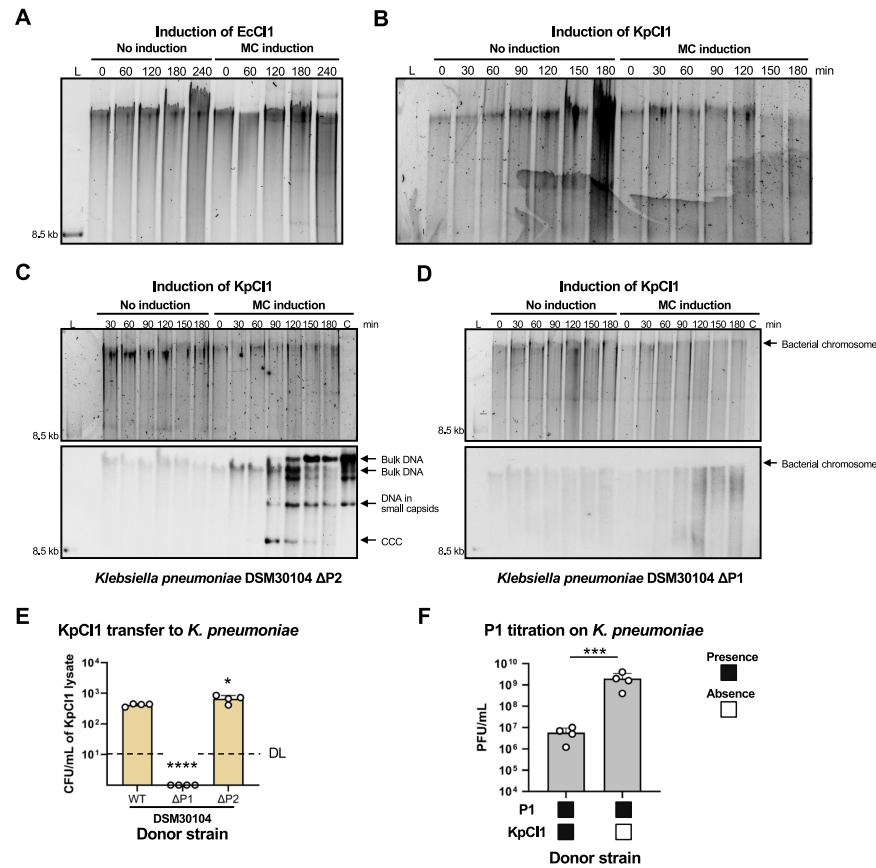


**Figure S2. Phage P1 induces KpCI1, related to Figure 1**

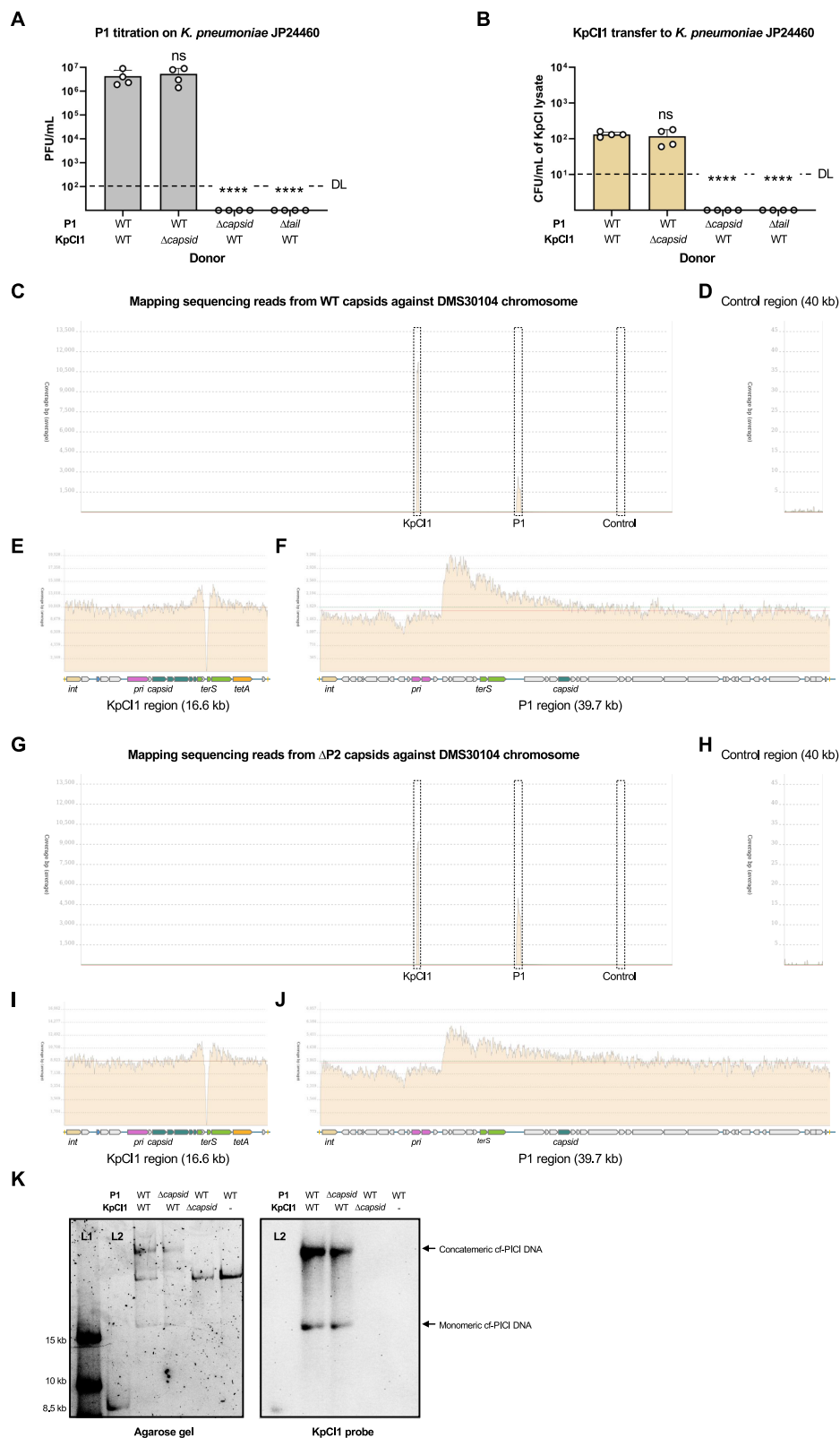
(A) Agarose gel for Figure 1B.

(B) Agarose gel for Figure 1C.

(C and D) *K. pneumoniae* DSM30104 strains mutant in P2 (C) or in P1 (D) were MC-induced, and samples were taken at the indicated time points (min) for DNA analyses. DNA was separated on a 0.7% agarose gel, followed by southern blotting analysis using a specific KpCI1 probe. L, southern blot molecular marker (DNA molecular weight marker VII; Roche); C, DNA extracted from capsid; CCC, covalently closed circular.

(E) Deletion of P1 abolished intraspecies KpCI1 transfer. The *K. pneumoniae* DSM30104 strains mutant in P1 or P2 were MC-induced, and the resulting lysates were tested for KpCI1 transfer, using *K. pneumoniae* JP24460 as recipient. Values are presented as means of CFU per milliliter of cf-PICl donor lysates. Error bars represent the standard deviation. After log<sub>10</sub> transformation, a one-way ANOVA was conducted followed by Dunnett's multiple comparisons test to compare the WT sample to other samples.  $n = 4$  independent samples.  $*p \leq 0.05$ .  $****p \leq 0.0001$ . WT, wild-type DSM30104 carrying both prophages P1 and P2;  $\Delta P1$ , DSM30104  $\Delta P1$ ;  $\Delta P2$ , DSM30104  $\Delta P2$ .

(F) KpCI1 interferes with P1 reproduction. DSM30104 derivative strains carrying P1, in the presence or absence of KpCI1, were MC-induced, and the P1 titer was quantified. Black boxes indicate the presence of P1 or KpCI1 in the donor strains. The recipient strain was *K. pneumoniae* JP24460, a derivative of the DSM30104 mutant in P1, P2, and KpCI1. Values are presented as means of plaque-forming units (PFUs) per milliliter of lysates. Error bars indicate the standard deviation. A t test was used to compare the data after log<sub>10</sub> transformation.  $***p \leq 0.001$ .  $n = 4$  independent samples.



(legend on next page)

### Figure S3. cf-PICs naturally produce tailless particles, related to Figure 2

(A and B) The low intraspecies transfer of KpCI1 was due to P1-mediated generalized transduction. Derivative *K. pneumoniae* DSM30104 strains carrying either WT P1, P1 mutant in the capsid, or tail genes and carrying either WT KpCI1 or its capsid derivative mutant were MC-induced, and the formation of P1 (A) or KpCI1 (B) infective particles was measured using *K. pneumoniae* strain JP24460 (a derivative of DSM30104 mutant in P1, P2, and KpCI1) as the recipient. After  $\log_{10}$  transformation, a one-way ANOVA was conducted, followed by Dunnett's multiple comparisons test to compare the WT DSM30104 sample to other samples.  $n = 4$  independent samples. ns,  $p > 0.05$ . \*\*\*\* $p \leq 0.0001$ . WT, wild-type element of P1 or KpCI1 in DSM30104 derivative strains. DLs, detection limits.

(C–J) KpCI1 DNA was packaged in capsids more extensively than P1 DNA. Capsid DNA was obtained from 35 mL induced cultures of WT *K. pneumoniae* DSM30104 (JP23778) or P2 mutant strains (JP24853) and sequenced by SeqCenter using Illumina short-read sequencing. Sequencing reads from WT (C–F) or P2 mutant (G–J) samples were mapped against the DSM30104 bacterial chromosome. The colored solid line represents the average (green) or the median (red) coverage per base pair (bp) across the mapped genome. A 40 kb bacterial chromosomal region not associated with KpCI1 or P1 was used as a control. WT, wild type. The experiment was performed with one replicate. (C) Mapping of capsid DNA from WT DSM30104 samples across the DSM30104 chromosome, with zoomed-in views of a control genomic region (D), the KpCI1 region (E), and the P1 region (F). (G) Mapping of capsid DNA from P2 mutant samples across the DSM30104 chromosome, with zoomed-in views of a control genomic region (H), the KpCI1 region (I), and the P1 region (J).

(K) The extensive packaging of KpCI1 DNA into small capsids is independent of the packaging of P1. Derivative *K. pneumoniae* DSM30104 strains, carrying different WT or capsid mutants of P1 or KpCI1, were MC-induced, the packaged DNA was extracted from the obtained lysates and separated on a 0.7% agarose gel (left panel), followed by a southern blotting analysis using a specific KpCI1 probe (right panel). A densitometric analysis of the southern blotting was performed using ImageJ. The mean grayscale values of lanes 1, 2, 3, and 4 are 199, 208, 232, and 233, respectively. Lower grayscale values indicate a more intense signal for the detected KpCI1 DNA. “–” indicates the absence of KpCI1 in the donor strain. WT, wild type; L1, invitrogen 1 kb plus DNA ladder; L2, southern blot molecular marker (DNA molecular weight marker VII, Roche).

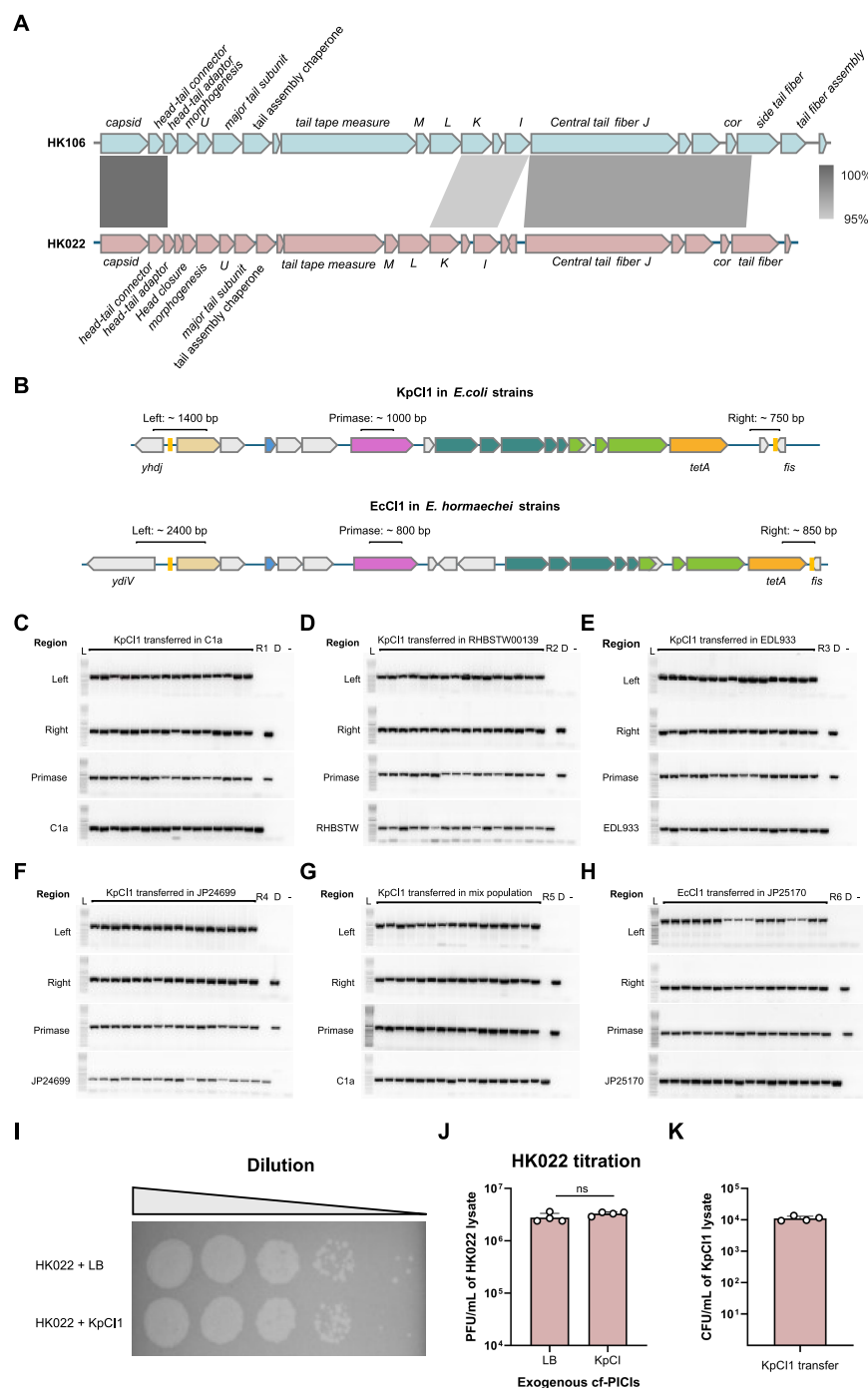


**Figure S4. PCR validation related to Figures 3, 4, and 5**

(A) Comparative maps of the tail region encoded by the HK022 and HK106 prophages. Gray scales between phage sequences indicate regions that share similarity based on BLASTn.

(B) Schematic maps of cf-PICIs in recipient strains. Top: diagram showing KpCI1 with a *tetA* cassette integrated into *E. coli* recipient strains. The integration site is flanked by *yhdJ* (specific to *E. coli* and absent in the *K. pneumoniae* donor) and *fis* (present in both donor and recipient strains, containing the KpCI1 attachment site). PCR target regions for (C)–(G) are marked.

Bottom: diagram of EcCI1 with a *tetA* cassette integrated into *E. hormaechei* recipient strains. Integration is flanked by *ydIV* (specific to *E. hormaechei* and absent in the *E. coli* donor) and *fis* (shared by both strains, containing the EcCI1 attachment site). PCR target regions for (H) are indicated.

(legend continued on next page)



(C–F) PCR validation of full KpCI1 transfer into *E. coli* strains: C1a (C), RHBSTW-00139 (D), EDL933 (E), and JP24699 (F). Primers amplified the “left,” “right,” and “primase” regions of KpCI1, along with the strain-specific chromosomal region. L, invitrogen 1 kb plus DNA ladder; R1–R4, recipient strains C1a, RHBSTW-00139, EDL933, and JP24699; D, *K. pneumoniae* DSM30104  $\Delta$ P2 donor strain (JP24853); “–”, negative PCR control.

(G) PCR confirmation of full KpCI1 transfer into *E. coli* JP24888 in mix population experiment. Primers targeted the “left,” “right,” and “primase” regions of KpCI1 and a JP24888-specific chromosomal region. L, invitrogen 1 kb plus DNA ladder; R5, JP24888 recipient; D, donor strain JP24853; “–”, negative control.

(H) PCR confirmation of EcCI1 transfer into *E. hormaechei* JP25170. Primers amplified the “left,” “right,” and “primase” regions of EcCI1 and a JP25170-specific chromosomal region.

L, invitrogen 1 kb plus DNA ladder; R6, JP25170 recipient; D, *E. coli* GN02175 donor strain (JP24927); “–”, negative control.

(I–K) KpCI1 uses the excess of tails produced after induction of the HK022 prophage. 10-fold dilutions of the HK022 lysate (maximum concentration:  $10^6$  PFU/mL) were mixed with KpCI1 ( $10^8$  particles/mL) or LB (as a control). The mixed lysates were then used to infect *E. coli* (I), and the number of plaques obtained was quantified (J). Values are presented as means of PFU per milliliter of HK022 lysates. Error bars indicate the standard deviation. A t test was used to compare the data after  $\log_{10}$  transformation. ns,  $p > 0.05$ .

(K) KpCI1 transfer obtained with the mix that contained the highest concentration of phage lysate ( $10^6$  PFU/mL). Values are presented as means of CFU per milliliter of KpCI1 lysates. Error bars indicate the standard deviation.  $n = 4$  independent experiments.

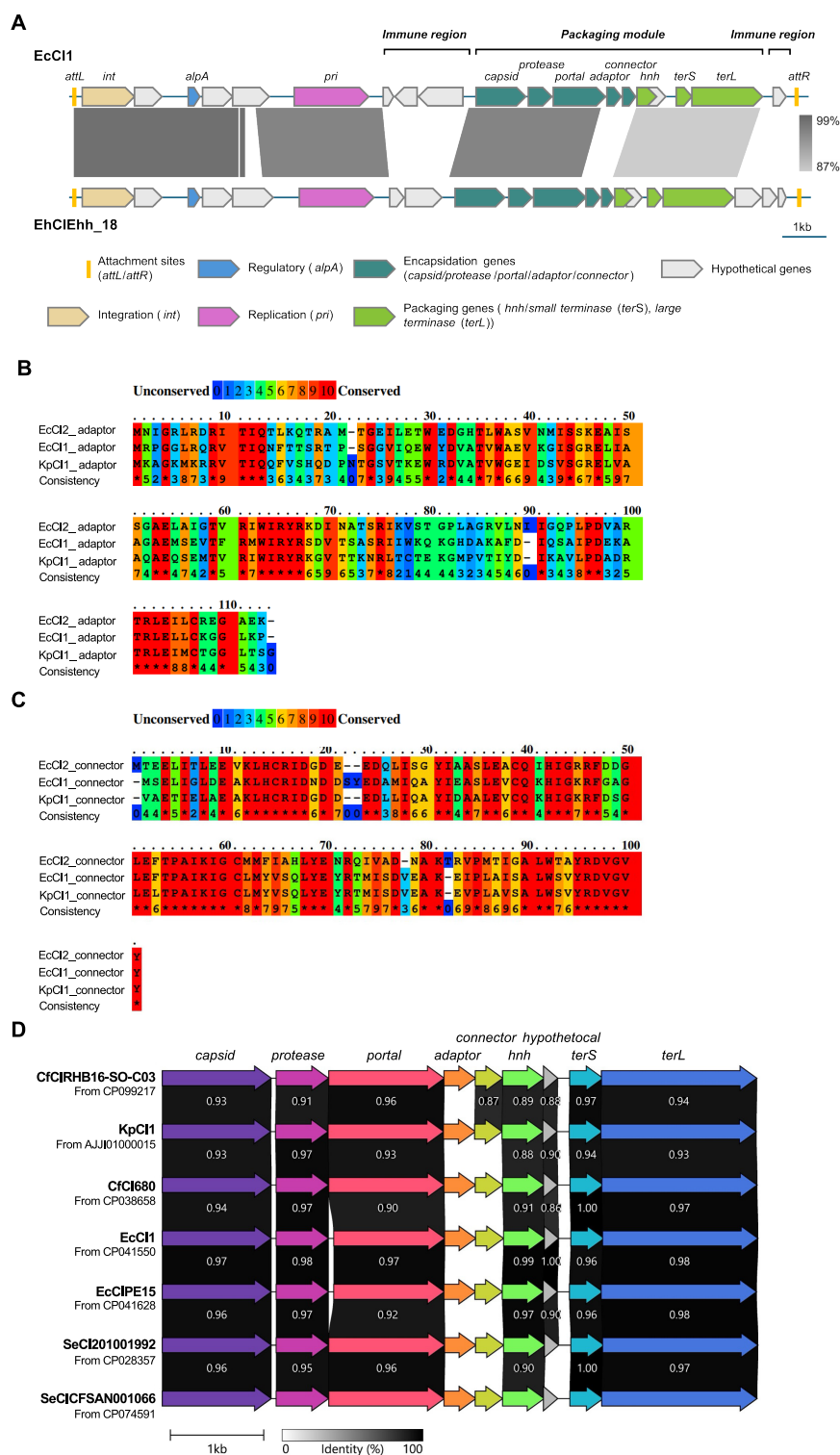


**Figure S5. The cf-PIC1-encoded tail adaptor and connector proteins determine tail specificity, related to Figure 5**

(A) Comparison between EcCI1 and EhCIHh\_18. A comparative map between cf-PICs EcCI1 and EhCIHh\_18. Genes are colored based on their function. Gray scales between cf-PIC1 sequences indicate regions that share similarity identified by BLASTn.

(B) PRALINE alignment for cf-PIC1 adaptors.

(C) PRALINE alignment for cf-PIC1 connectors.

In (B) and (C), colors represent the conservation between amino acids.

(legend continued on next page)

---

(D) Gene cluster comparison of the packaging modules among cf-PICs. The figure represents cf-PICs carrying almost identical packaging modules but different adaptor and connector genes. Arrows indicate phage structure proteins. Gray scales between phage sequences indicate the regions share similarity. The cutoff considered for the identity is 86%, and the identity of 87%–100% was considered as high identity in the packaging module. Comparison and visualization were performed by Clinker.

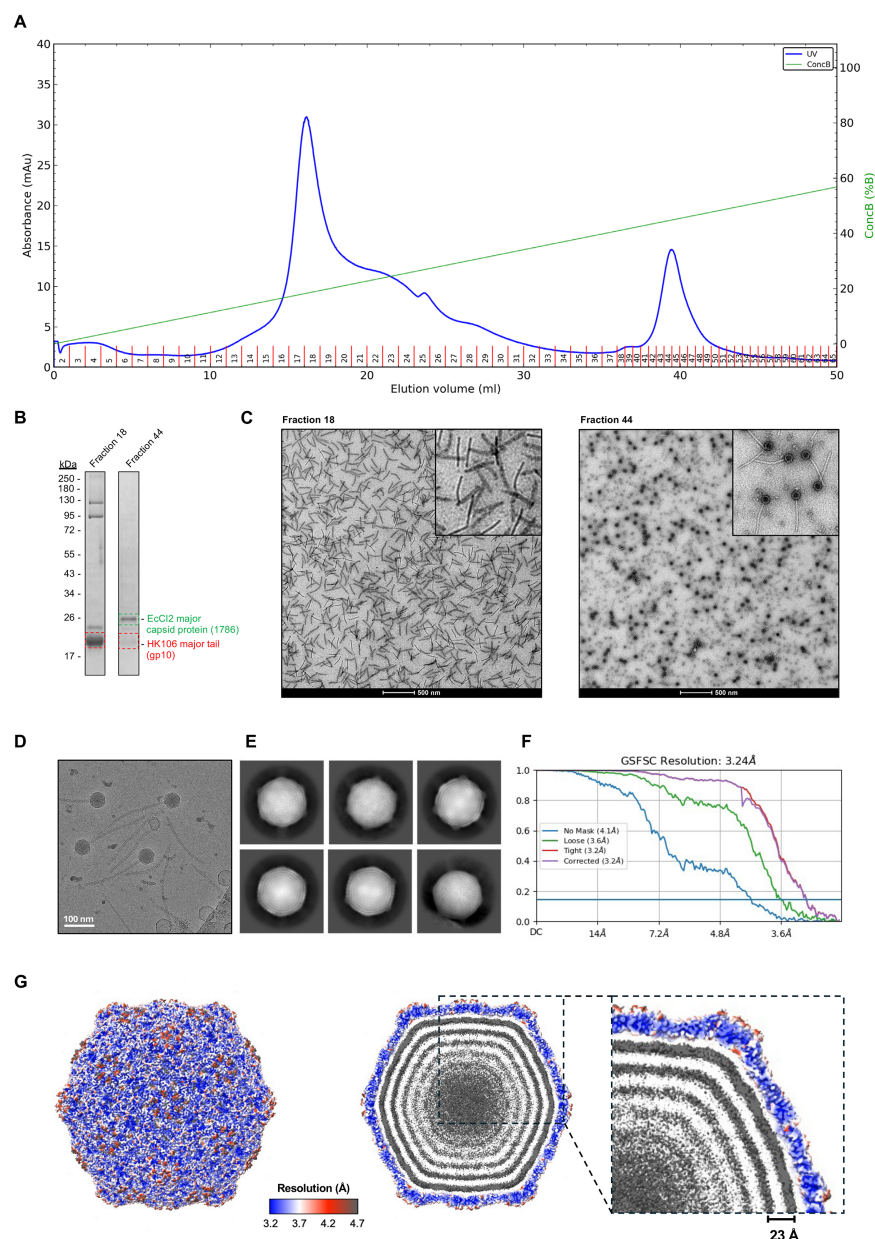


**Figure S6. Purification of EcCl2 via ion-exchange chromatography and EcCl2 capsid reconstruction, related to Figure 6**

(A) After initial purification by CsCl density gradient centrifugation, EcCl2 virions were subjected to anionic exchange chromatography on a HiTrap Q HP Cytiva column to remove the excess unbound tails of the helper phage HK106. The chromatography was conducted at pH 8.4 in a gradient of buffer B containing 2 M NaAc relative to buffer A devoid of NaAc, resulting in two distinct peaks on the chromatogram.

(B) Left: the first peak corresponding to low salt elution was subjected to SDS-PAGE, and the representative fraction 18 is shown, revealing the presence of major tail protein (gp10) of phage HK106. Right: SDS-PAGE of the second peak, corresponding to high salt elution. The representative fraction 44 is shown, revealing the presence of both the EcCl2 cf-PIC1 capsid and the major tail protein. Gels were cropped to represent only the fractions imaged in (C).

(C) Fractions 18 and 44 were subjected to negative-stain EM, visualizing the free HK106 tails and assembled EcCl2 cf-PIC1 particles, respectively. Scale bars represent 500 nm.

(D) Representative cryo-EM micrograph obtained during data collection of the EcCl2 capsid.

(E) 2D classes of the EcCl2 capsid used for 3D reconstruction.

(F) Fourier shell correlation (FSC) curves of the 3D reconstruction map.

(G) Local resolution of the EcCl2 capsid map, with the genome layers distance labeled.



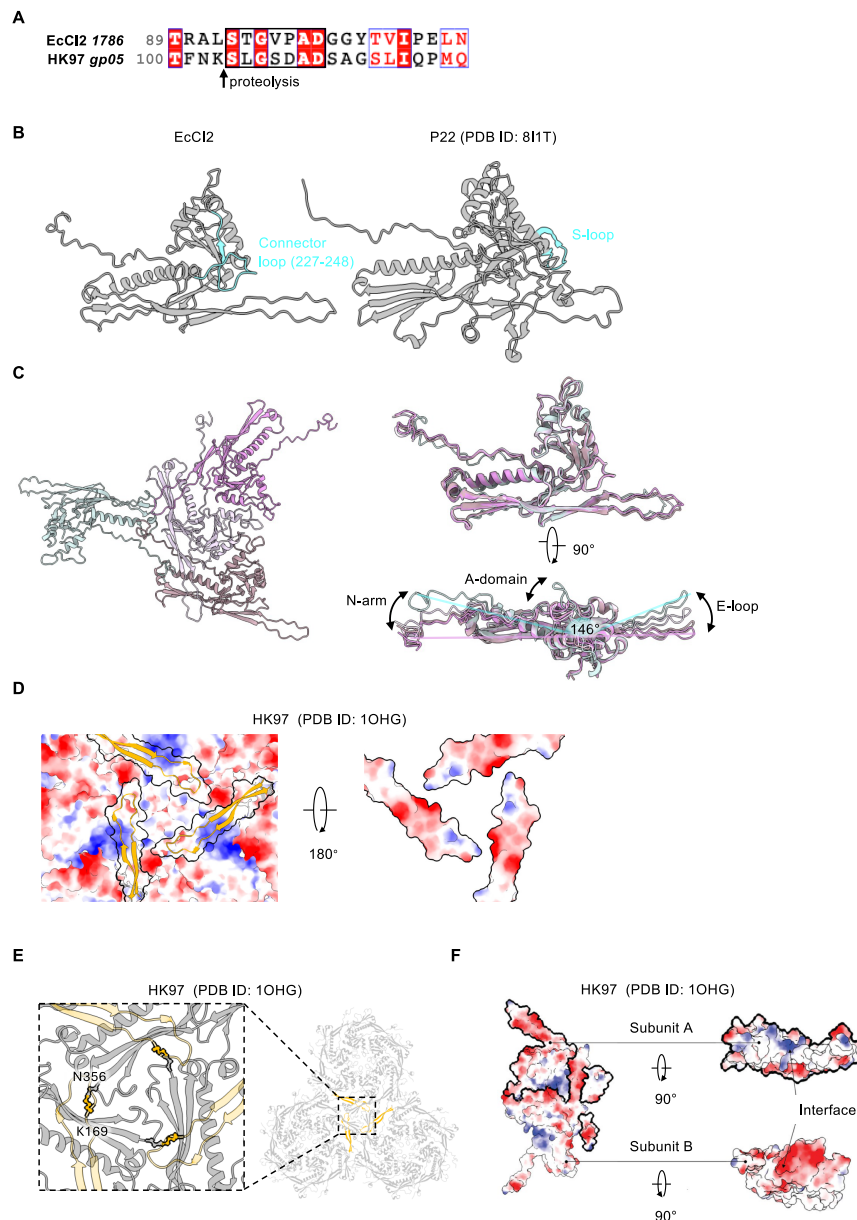


**Figure S7. Topology of MCP and structural comparisons to MCPs of phages P22 and HK97, related to Figures 6 and 7**

(A) Amino acid alignment of mature MCP of EcCl2 and HK97. The N termini of both MCPs start with a conserved sequence [SxGxxAD], with x denoting any residue, which suggests a shared proteolysis mechanism.

(B) The connector loop is localized between residues 227–248 (cyan) present in EcCl2 MCP. It is localized similarly—relative to the topology of the entire MCP—to the capsid size and symmetry determination loop (S loop) of the P22 bacteriophage (PDB: 8I1T).

(C) Left: ribbon representation of the ASU, showing the four MCPs. Right: overlay of all the MCPs in the ASU, showing variation primarily in three sites: the N arm, A domain, and E loop. It results in different angles between the E loop and N arm, causing the penton MCP (mint green) to be the narrowest at an angle of 146° between the E loop and N arm, whereas the MCP from the hexon (shades of pink) being flatter, nearing a 180° angle between the E loop and N arm.

(D) Electrostatic surface potential at the 3-fold axis of the HK97 capsid (PDB: 1OHG) except for E loops (orange ribbon), for which only outlines are shown. The E loops are shown on the right, rotated 180°.

(E) In HK97, the interaction between three hexons includes the formation of a crosslink between the N arm and P domain of the neighboring hexon between residues K169 and N356.

(F) Within a capsomer, interactions between two HK97 subunits are established by complementary patches at the two faces of the MCP.

In electrostatic representations, the negative potential (red) corresponds to negatively charged residues, while positive potential (blue) indicates positively charged residues. Neutral regions are shown in white.

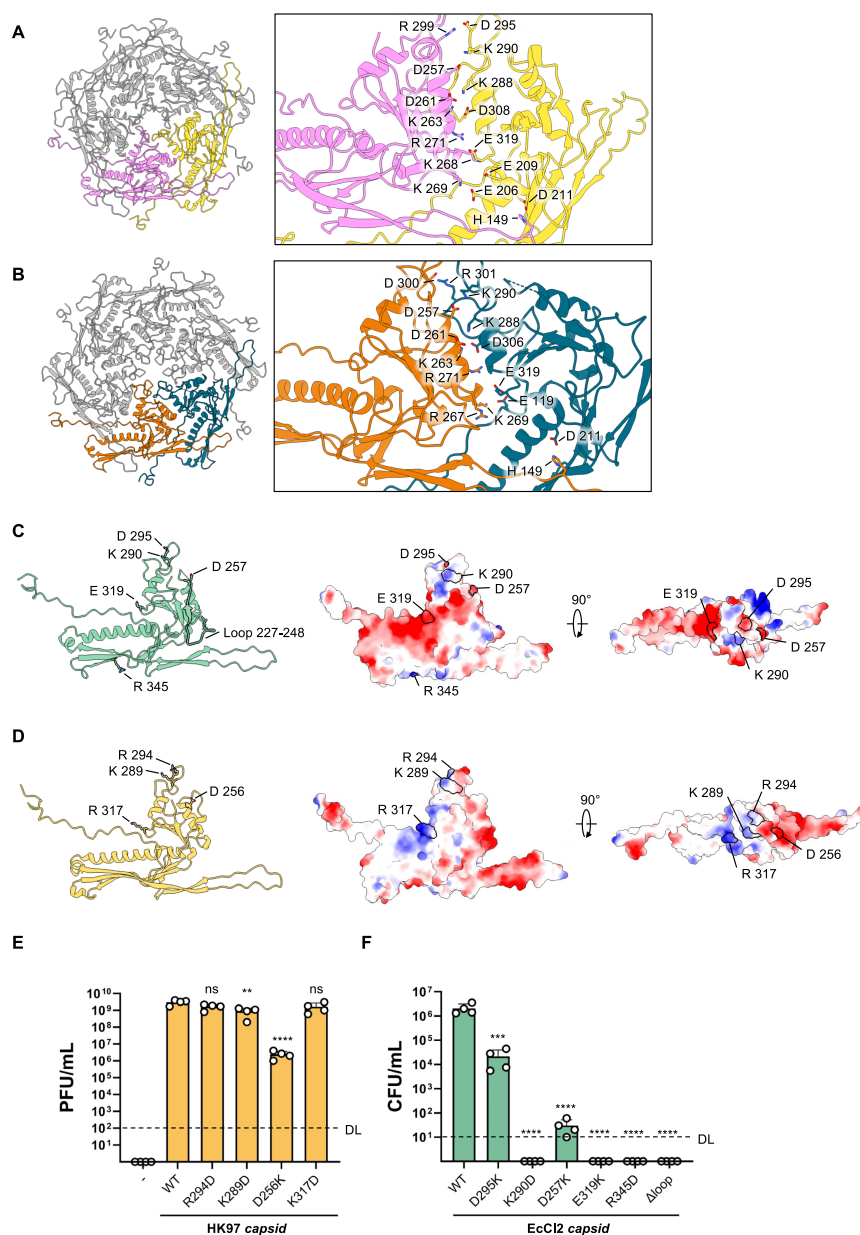


**Figure S8. Salt bridges at the intracapsomer interface and unique interactions of a single MCP, related to Figure 7**

(A and B) Salt bridges formed between two MCPs within a penton (A) and hexon (B) are shown, with the specific interacting residues highlighted.

(C and D) Representation of the residues involved in the formation of salt bridges in EcCl2 MCP (C) and the corresponding residues in HK97 MCP (PDB: 1OHG) (D), together with the representation of their electrostatic potential. Negative potential (red) corresponds to negatively charged residues, while positive potential (blue) indicates positively charged residues. Neutral regions are shown in white.

(E) HK97 capsid mutagenesis affected phage capsid formation. The strain carrying an HK106 prophage mutant in its capsid gene was complemented with the pBAD18 empty vector (-) or with different versions of the HK97 capsid gene, which express mutations in residues potentially important for the formation of the capsid. Samples were induced with 2  $\mu$ g/mL MC and 0.02% L-arabinose. The resulting filtered lysates were tested for phage titration, using the *E. coli* 594 strain expressing the WT HK97 capsid gene as recipient. Values are presented as means for the PFU per milliliter of lysates. Error bars indicate the standard deviation. A one-way ANOVA with Dunnett's multiple comparisons test was used to compare the data between samples with the WT HK97 capsid and the other samples after  $\log_{10}$  transformation. ns,  $p > 0.05$ . \*\* $p \leq 0.01$ . \*\*\*\* $p \leq 0.0001$ .  $n = 4$  independent samples.

(F) EcCl2 mutagenesis abolished EcCl2 transfer. Derivative strains lysogenic for HK106 and carrying either EcC2 or derivative mutants of this island encoding variants of the EcCl2 capsid gene were MC-induced, and the transfer of the WT and mutant islands was analyzed. Values are presented as means for the CFU per milliliter of lysates. Error bars indicate the standard deviation. A one-way ANOVA with Dunnett's multiple comparisons test was used to compare the data between samples with the WT EcCl2 capsid and the other samples after  $\log_{10}$  transformation. \*\*\*\* $p \leq 0.0001$ .  $n = 4$  independent samples. DLs, detection limits.